

POLITECNICO DI TORINO

Master's Degree in Nanotechnologies for ICTs



Master's Degree Thesis

Electric field control of topological Weyl semimetals

Supervisor

Prof. Renato GONNELLI

External supervisor

Dr. Cezar ZOTA

Candidate

Alberto FERRARIS

September, 2021

Summary

Weyl semimetals are a recently discovered class of materials that present unique topological properties. In the last years, they have been a topic of great interest for research, but few applications have been proposed to exploit their unique characteristics.

The transport properties of Weyl semimetals make them very promising for applications in electronics, especially at low temperatures. This work is focused on the interaction of these materials with an electric field, with the aim to study the behavior of gated devices with a Weyl semimetal channel.

The first model studied was the one of a Klein tunneling transistor, a device where the effect of the gate is to shift the energy bands of a portion of the channel, creating an energy barrier that reflects some of the incoming carriers. This model was improved by adding the screening effect of the potential applied by the gate electrode inside the material, and showing that this effect is playing an important role in the modulation of the current passing through the device.

The next step was studying more in detail the screening effect in Weyl semimetals, to improve the accuracy of the previous model, as well as future models of field-effect devices. A screening model was developed, taking into account the contribution of both the bulk and surface states of the material. This model provides information on the potential decay as we move deeper into the material, and on the excess charges that are accumulated inside it.

Finally, the fabrication process that leads to the realization of test devices is explained. The measurements obtained from these devices will be a way to test the results of the presented models, providing insights on the properties of the materials and on the next steps needed to realize transistors with good performances.

Acknowledgements

During the realization of this thesis I received support and advice from many people.

I would first like to express my sincere gratitude to Cezar Zota and Lorenzo Rocchino, who constantly helped me in my work and provided me with invaluable feedback.

I am also deeply grateful to my supervisor, Professor Renato Gonnelli, who agreed to help me during this thesis and provided me with very useful advice.

I want to thank all the people from the MIND group and the SCHINES project, who made me feel at home, even if, due to the current events, we rarely were able to meet.

I would also like to thank my family for the continuous support they gave me during my studies and for the love they showed me when I was far away from home.

Finally, I would like to thank my friends, the ones I have in Italy, the ones I met in Switzerland and especially the ones that came here and shared with me this experience.

I wish to thank you all, as without you, all this would have not been possible.

Table of Contents

1	Introduction	1
1.1	Topological materials	1
1.1.1	Topological insulators	1
1.1.2	Weyl Semimetals	2
1.1.3	Dirac Semimetals	4
1.2	Properties of Weyl semimetals	5
1.2.1	Weyl nodes and topological protection	5
1.2.2	Type-I and type-II Weyl semimetals	7
1.2.3	Fermi arcs	7
1.3	Overview and purpose of this thesis	10
2	Klein tunneling Weyl semimetal transistor	12
2.1	Klein Tunneling effect	12
2.2	Field effect devices using Klein tunneling	13
2.2.1	Device geometry	14
2.2.2	Scattering against the barrier and critical angle	16
2.2.3	Transmission probability	18
2.2.4	Current through the potential barrier	20
2.3	Screening effect in a Klein tunneling transistor	21
2.3.1	Voltage profile in the Weyl semimetal channel	22
2.3.2	Current computation	23
3	Screening in Weyl semimetals	29
3.1	Previous works on screening	29
3.2	Material model	30
3.3	Physical approach	31
3.3.1	Lattice permittivity	33
3.4	Surface and bulk charge densities	34
3.4.1	Bulk states	34
3.4.2	Chemical potential	35
3.4.3	Fermi Arc states	36

3.5	Boundary Conditions	37
3.6	Solution of the Poisson equation	39
3.7	Results	39
3.7.1	Ideal conditions	39
3.7.2	Effect of the Fermi level	44
3.7.3	Effect of the Temperature	47
3.7.4	Effect of the distance between the Weyl nodes	49
3.7.5	Gate capacitance computation	50
3.7.6	Applications of the screening model	52
4	Fabrication of test devices	54
4.1	Challenges in the fabrication of Weyl semimetal crystals	54
4.2	Description of the fabrication process	55
5	Conclusions	59
A	Numerical methods used to solve the Poisson differential equation	62
A.1	Solution as a series of Initial Value Problems	62
A.2	Direct solution of the Boundary Value Problem	65
	Bibliography	66

Chapter 1

Introduction

1.1 Topological materials

Topology is a branch of mathematics that studies the properties of an object that are not altered by continuous deformations. Such properties are called topological properties, and can be used to classify the objects in a way that does not depend on their exact shape.

The first people who used topology to describe the properties of a material were David J. Thouless, F. Duncan M. Haldane and J. Michael Kosterlitz, who studied the electronic and magnetic properties of thin layers of matter, that were found to change as integer steps [1]. These studies attracted the interest of the scientific community, and they were awarded the Nobel Prize in Physics in 2016. Following their work, other studies have applied topology to explain the properties of other kinds of materials, including three-dimensional solids. The materials whose properties are well described by topology are called Topological materials.

The main examples of three dimensional topological materials are Topological insulators, Weyl semimetals and Dirac semimetals [2].

1.1.1 Topological insulators

Topological insulators are materials with a gapped band structure, despite having a gapless spectrum of states at their boundaries. The presence of these surface states is a direct consequence of the non-trivial topology of the band structure. The double-nature of this materials gives rise to the coexistence of both an insulating bulk and a metal-like surface [3].

The surface states present a linear dispersion relation, and have the shape of a bi-dimensional cone in momentum space, called Dirac cone. Moreover, they

are said to be topologically protected, meaning they are robust against any local perturbation [3].

A scheme of the band structure of a Topological insulator is shown in Figure 1.1.

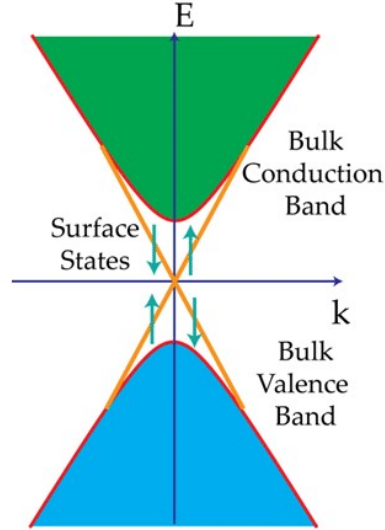


Figure 1.1: Qualitative scheme of the band structure of a Topological insulator. Taken from [4].

Topological insulators can be observed in materials with a strong Spin Orbit Coupling, which is the magnetic interaction between a particle's spin and orbital components as it travels in a potential. Its effect is to alter the energy levels of the electrons depending on their spin orientation.

Examples of Topological insulators are Bi_2Te_3 , Sb_2Te_3 and Bi_2Se_3 [5].

1.1.2 Weyl Semimetals

A semimetal is a material where the valence and conduction bands have a small overlap, that produces a small density of states around the Fermi energy [6].

In a Weyl semimetal, the two bands touch in a set of discrete points of the Brillouin zone, called Weyl nodes. These points are said to be topologically protected, meaning that their presence is due to the intrinsic topology of the Hamiltonian and, as a result, they cannot be removed by small perturbations [7].

The topological invariant associated to Weyl nodes is the so-called Berry curvature, a quantity related to the Berry phase, which is the extra phase accumulated by the evolution in time of an electronic wavefunction that is solution to a time-dependent Hamiltonian [4]. The Berry curvature acts similarly to a magnetic field

in momentum space, and it has been shown that Weyl nodes act as monopoles of the Berry curvature that can have a positive or negative charge, called chirality [2]. The Weyl nodes always appear in pairs, where one node is a source and the other a sink of Berry curvature, so that if we consider the entire Brillouin zone the total chirality is zero [7].

Another peculiar characteristic of Weyl semimetal are their topologically protected surface states, called Fermi Arcs, which present an open Fermi surface that connects the surface projections of the Weyl nodes [8]. A qualitative scheme of the Weyl semimetal band structure is shown in Figure 1.2.

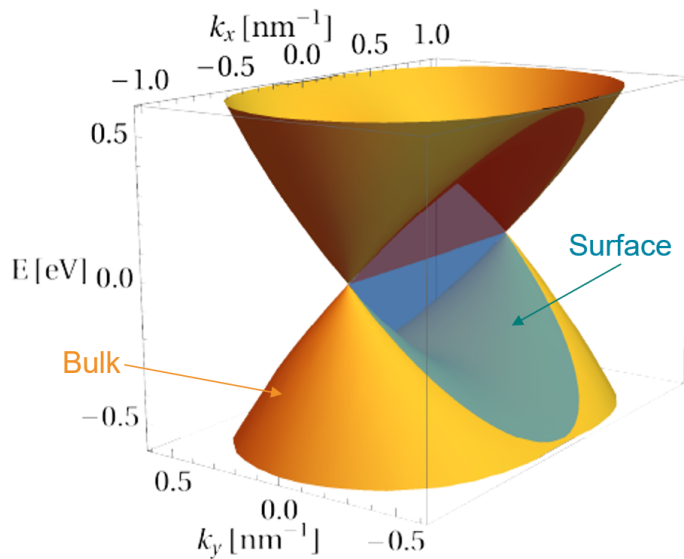


Figure 1.2: Scheme of the bands of a Weyl semimetal. Both the bulk bands in the proximity of a couple of Weyl nodes of opposite chirality and the corresponding Fermi Arc surface states are shown. Adapted from [9].

The presence of linear bands and the topological surface states provides Weyl semimetals with extremely high values of conductivity and carrier mobility, especially at low temperatures [10, 11].

Some examples of Weyl semimetals are TaAs, NbP [12], Ag₂S [13], MoTe₂, WTe₂ and WP₂ [14]; some of these, like WP₂ present a Weyl semimetal phase only in one of their possible crystal structures.

The most important characteristics of Weyl semimetals will be further explained in Section 1.2.

1.1.3 Dirac Semimetals

A Dirac semimetal is very similar to a Weyl semimetal, and also has band touching points that take the name of Dirac nodes. There are many ways a Dirac semimetal can be obtained, which result in materials with slightly different properties [7]. In some of these materials, the Dirac node can be seen as the superposition of two degenerate Weyl nodes of opposite chirality. This means that its total chirality is zero, and as a result it does not have the same topological protection as a Weyl node. It has been shown that a Dirac node of this kind can be split into a couple of Weyl nodes if a magnetic field is applied [15].

Similarly to Weyl semimetals, also some Dirac semimetals present conductive surface states, and in some cases they can be topologically protected, like the Fermi arcs [16].

Some examples of Dirac semimetals are Cd_3As_2 [17] and ZrSiS [18].

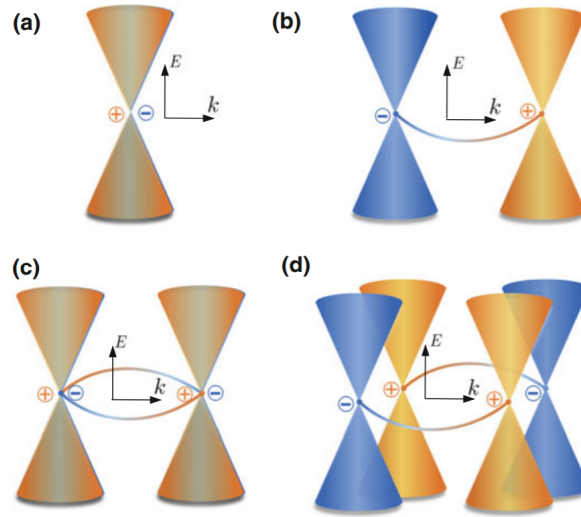


Figure 1.3: Band structure of Dirac and Weyl semimetals: (a) represents a Dirac semimetal with no topological surface states, (b) a Weyl semimetal with a single Fermi Arc, (c) a Dirac semimetal with two Fermi arcs, (d) a Weyl semimetal with two Fermi arcs. The plus and minus signs represent the positive or negative chirality of the bands. Taken from [16].

1.2 Properties of Weyl semimetals

1.2.1 Weyl nodes and topological protection

A material is a Weyl semimetal if its bands are non-degenerate and they touch in a set of few discrete points, called Weyl nodes. The conditions for band degeneracy are determined by the symmetry of the system: in most cases the bands are doubly degenerate, so to have bands that are typically non-degenerate instead, Spin orbit coupling must be non negligible and one between Time Reversal and Inversion symmetry must be broken¹.

The topological protection of the Weyl nodes can be explained starting from the fact that under these conditions the effective Hamiltonian of two energy states can be written in the form [7]:

$$H(\mathbf{k}) = f_0(\mathbf{k})\mathbb{I} + f_x(\mathbf{k})\sigma_x + f_y(\mathbf{k})\sigma_y + f_z(\mathbf{k})\sigma_z \quad (1.1)$$

where the terms f_i are real functions and σ_x , σ_y and σ_z , are the three Pauli matrices.

$$\sigma_x = \begin{bmatrix} 0 & 1 \\ 1 & 0 \end{bmatrix}, \quad \sigma_y = \begin{bmatrix} 0 & -i \\ i & 0 \end{bmatrix}, \quad \sigma_z = \begin{bmatrix} 1 & 0 \\ 0 & -1 \end{bmatrix}, \quad (1.2)$$

For the two states to touch we need $f_x = f_y = f_z = 0$ while f_0 only affects the distance from the Fermi energy. The set of points where each of these three functions are zero is a 2D surface in the momentum space, so the region where this condition is satisfied will be the intersection of these three surfaces that is usually a single point, representing our Weyl node. If this is the case for our material, then when a perturbation is added to the Hamiltonian and some of the terms are slightly modified, the result is that the intersection will be shifted in momentum space, but it will still be formed by one single point.

This topological protection is a peculiar characteristic that distinguishes Weyl semimetals from other materials with a similar band structure. One example is Graphene, a two-dimensional material with a similar dispersion relation, that however has not the same topological protection, as the Hamiltonian describing it includes only two of the Pauli matrices. For this reason, a band gap can be obtained if the Hamiltonian is perturbed [19].

Weyl semimetals take their name from the Weyl equation, which is a simplification of the relativistic Dirac equation for the case of massless particles. In fact, the Weyl equation well describes the quasi-particles formed by excited electrons with a \mathbf{k} vector close to the one of a Weyl node. We can get to it by Taylor expanding the

¹Time Reversal symmetry and Inversion symmetry are the properties of the system to remain invariant if the time and space coordinates are inverted.

generic expression of the Hamiltonian provided by Equation 1.1, in the proximity of the Weyl point that we assume to have position $\mathbf{k} = 0$ in momentum space. We can assume f_0 to be negligible, in this case the energy of the Weyl node would almost coincide with the Fermi energy. This is because our material has to be a semimetal, meaning that the Weyl node must be located between the valence and conduction bands. By doing so we get [7]:

$$H(\mathbf{k}) \simeq \sum_{a=x,y,z} \nabla_k f_a(\mathbf{k})|_{\mathbf{k}=0} \cdot \mathbf{k} \sigma_a = \sum_{a=x,y,z} \mathbf{v}_a \cdot \mathbf{k} \sigma_a \quad (1.3)$$

where \mathbf{v}_a are the effective velocities. In the case where $\mathbf{v}_a = v_F \hat{a}$, meaning that we have a constant Fermi velocity in all directions, the Weyl equation is obtained:

$$\mathbb{I} \frac{1}{v_F} \frac{\partial \psi}{\partial t} + \sigma_x \frac{\partial \psi}{\partial x} + \sigma_y \frac{\partial \psi}{\partial y} + \sigma_z \frac{\partial \psi}{\partial z} = 0 \quad (1.4)$$

The solutions of the Weyl equation are called Weyl spinors, and are written in the following form:

$$\psi(\mathbf{r}, t) = \chi e^{\frac{\mathbf{p} \cdot \mathbf{r} - Et}{i\hbar}} \quad (1.5)$$

where \mathbf{p} and \mathbf{r} are the momentum and position operators, E is the eigenvalue of the energy, t is the time and χ is a two-component spinor wavefunction.

The states described by the Weyl equation are called Weyl fermions and are particles with no mass and a half-integer spin. Massless particles have a linear dispersion relation, meaning that the Weyl equation well describes our material only in the region of momentum space where the bands are linear and their shape can be approximated to a cone.

The most important consequence of the linear dispersion relation of the bands, close to the Fermi level, is the fact that the Fermi velocity of the carriers is constant, and can have particularly high values [20], granting these materials very good transport properties.

Because of the linear dispersion relation, the density of states of an ideal Weyl cone with a non-tilted axis, is the following:

$$D(E) = \frac{E^2}{\pi^2 v_F^3} \quad (1.6)$$

This expression tends to zero as the value of the energy tends to zero, which represents the energy of the Weyl node. For this reason, even if the valence and conduction bands touch, there is an energy region where very few states are allowed, making the material behave differently from a metal. It has been shown that the density of states tends to zero at the Weyl nodes even in the presence of a weak disorder in the crystal lattice [21].

1.2.2 Type-I and type-II Weyl semimetals

In the first discovered Weyl semimetal, TaAs [22], the bands have the shape of cones that are straight, with their main axis parallel to the energy axis. However, in most materials, the cones may be tilted, meaning that the slope of the bands and thus the Fermi velocity is not the same in all directions. As a result, materials with tilted Weyl cones will be anisotropic. This small tilt does not alter the properties of our material qualitatively, so all these materials can be grouped into the family of type-I Weyl semimetals.

A significant change happens when the Weyl cones reach a critical tilt angle, so that the outer surface of the cones crosses the vertical axis. In this case, the Fermi level will cross both conduction and valence band, and thus the Fermi surfaces at the energy of the Weyl nodes will no longer be a point but will open outwards starting from the node. As a result, the material will have electron and hole pockets in the proximity of the Weyl nodes. Materials that have this kind of property are called type-II Weyl semimetals (MoTe₂, WTe₂ and WP₂ belong to this class [14]).

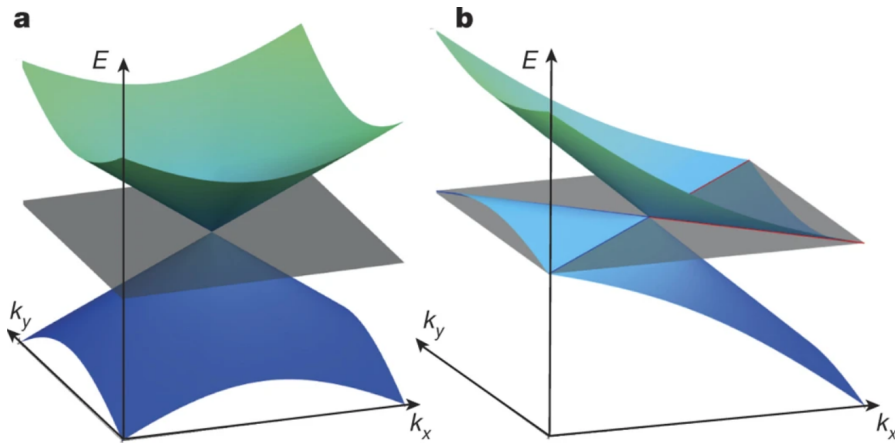


Figure 1.4: Comparison between the band structure of a type-I Weyl semimetal, shown in panel (a), and a type-II Weyl semimetal, in panel (b). The grey plane represents the surface at constant energy that is the Fermi energy. Taken from [23].

1.2.3 Fermi arcs

All Weyl semimetals present a set of states on their surface, that take the name of Fermi Arcs. The origin of the name comes from the fact that, differently from the states found in ordinary materials, they have an open Fermi surface that describes an arc in momentum space, connecting the surface projections of two Weyl nodes with opposite chirality [8].

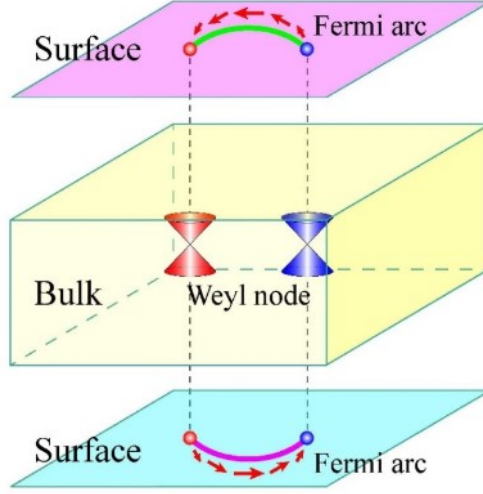


Figure 1.5: Scheme of the bands of a Weyl semimetal. Both the bulk bands in the proximity of a couple of Weyl nodes of opposite chirality and the corresponding Fermi Arc surface states are shown. Taken from [22].

Fermi Arcs can be studied theoretically as states that reside at the interface between the Weyl semimetal and a medium representing either vacuum or a trivial insulator. It is possible to model this interface with a linear interpolation of the Hamiltonian of the two materials [20]. This means writing a single parameter-dependent Hamiltonian that describes both phases, and that contains one parameter that varies as we move into space from one material to the other [24]. One example of such Hamiltonian is the following, that can describe both a Weyl semimetal with two Weyl nodes and a trivial insulator depending on the value of Δ [20].

$$H = \left(\frac{k_z^2}{2m} - \Delta \right) \sigma_z + v_F (k_x \sigma_x + k_y \sigma_y) \quad (1.7)$$

In this equation v_F is the Fermi velocity, and $m = (\kappa + v_F \Delta k_0 / 2) / 2v_F^2$ is a parameter that takes into account the curvature of the bands as we move away from the Weyl nodes [20]. The space-dependent parameter Δ assumes a fixed positive value in the WSM phase and a negative one in the insulator; in the interface layer, Δ changes linearly between those values. It has also been proven that the properties of the surface states should not change even if the potential at the interface varies differently or fluctuates [20]. The physical meaning of Δ is both the position in energy of the saddle point of the WSM bands, when it is positive, and the energy gap of the insulating phase when it is negative (taken with positive sign). This Hamiltonian can be solved in order to find the eigenfunctions that are bound to the

surfaces of the WSM. We can make the assumption that the interface between the two materials is abrupt, which means that the interpolating layer between them has a thickness smaller than every other length in the system. The solution we obtain in this case is [20]:

$$\psi = \sqrt{\frac{(\Delta k/2)^2 - k_z^2}{mv_F}} \begin{pmatrix} 0 \\ 1 \end{pmatrix} e^{\frac{k_z^2 - (\Delta k/2)^2}{2mv_F} x} \quad (1.8)$$

where Δk represents the distance between the Weyl nodes and $k_z \in [-\Delta k/2, \Delta k/2]$. The Fermi Arc wavefunction is confined at the interface, as its amplitude decreases exponentially when we move away from its position ($x = 0$).

The dispersion relation of these states is $\varepsilon(k_y, k_z) = v_F k_y$. We can see how the energy depends only on the y component of the momentum, which means that in this model the Fermi Arcs will be straight lines parallel to the z axis in momentum space.

Although in this model Fermi Arcs have take the form of straight lines, their shape and length greatly varies between the different materials: some of them like TaAs and NbAs present short and curved Fermi Arcs, while in Ta₃S₂ they are long and straight, and in HgTe they have a large circular shape [25]. For this reason it is hard to find a unique description of them and of their properties.

The states bound to the opposite surface of the material have opposite values of both spin and k_z , meaning that they will propagate in the opposite direction [26]. We also know that the topological protection of these states tends to inhibit the scattering processes, and that their main source of dissipation is the interaction with the bulk states of the material [13].

Fermi Arc states have been observed by Angle-Resolved Photoemission Spectroscopy (ARPES), a characterization technique that exploits the photoelectric effect to map the electronic band structure at the surface of a material [27]. This is currently one of the most effective ways to verify if a material is a Weyl semimetal. Figure 1.6 shows an example of the observation of Fermi Arc states using ARPES.

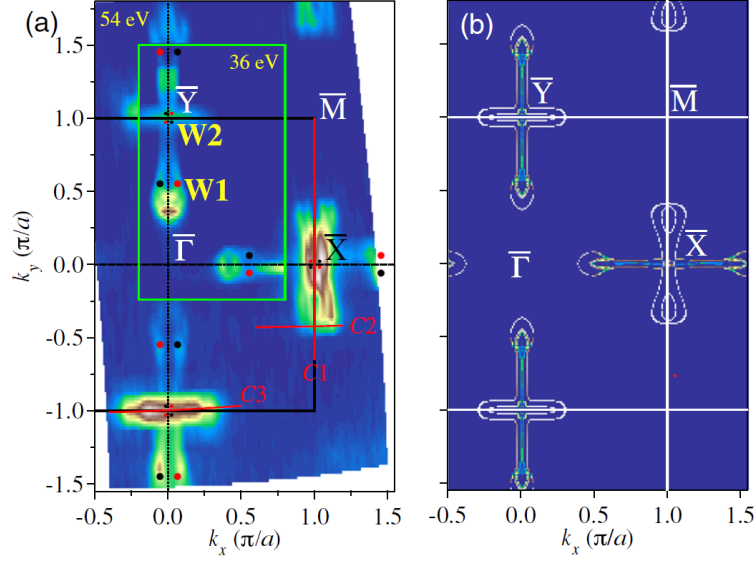


Figure 1.6: (a) Photoemission plot showing the density of states at the surface of the Weyl semimetal TaAs. (b) Theoretical computation of the Fermi Arc surfaces. Taken from [27].

1.3 Overview and purpose of this thesis

In the last years topological semimetals have caught the attention of many researchers and a lot of effort has been done to find which materials are part of this class. In fact, as we have seen in this chapter, their properties are peculiar and not completely understood, which makes them a very interesting topic of research.

However, up to now very few applications have been proposed to exploit their unique properties. Therefore, one of the objectives of this thesis is to study novel devices realized with this kind of materials. In particular, their transport properties make them very promising for applications in electronics, especially at low temperatures, as the high mobility typical of these materials could provide better performances at high frequencies [11].

In this work, we will focus on the interaction of these materials with an electric field, in order to model field-effect devices that exploit the properties of Weyl semimetals. These devices use the potential applied on the gate electrode as a mechanism to control the current passing through the channel. In Chapter 2 we will show the concept of Klein tunneling transistor where this is achieved by creating a potential barrier, able to reflect a portion of the carriers. We will then show the importance of the screening effect on the performance of the device and we will focus more in detail on the interaction between the material and the electric field,

providing a more accurate description of the screening effect, which is particularly useful in the realization of precise device models of field-effect transistors. Finally, we will describe the work done towards the fabrication of such devices, which will allow to test the models experimentally.

For our studies we will focus on the family of type-I Weyl semimetals, as their reduced density of states close to the Weyl nodes is more suited for this application. The results obtained could also be used to describe some Dirac semimetals, which present similar properties [4].

Chapter 2

Klein tunneling Weyl semimetal transistor

In this section the concept of the Klein tunneling effect is described and it is shown how it can be used to make a field-effect transistor, based on the information found on the literature [28, 29, 30].

The concept device will have a Weyl semimetal channel and a metallic gate, with an oxide layer in between them. The effect of the potential applied on the gate is to locally shift the energy of the bands in the region underneath it, creating a potential barrier for the carriers to overcome. The transmission of the carriers through this barrier is described by the Klein tunneling effect, and determines the properties of the device.

Then this model will be improved, to take into account the fact that the external potential applied by the gate of the device is screened by the charges present in the Weyl semimetal channel. This will allow us to see how this effect alters the behavior of the device.

2.1 Klein Tunneling effect

The Klein paradox is a process in relativistic physics where an incoming electron penetrates through an energy barrier that exceeds its energy. In this case the transmission probability of the particle increases for higher barriers, and the barrier tends to be perfectly transparent as its energy tends to infinity [31]. This result is counter-intuitive, since in conventional quantum mechanics the transmission probability should decrease exponentially as the energy of the barrier increases.

This difference can be explained by the fact that a very strong potential barrier can generate positron states that are in the same energy range as the electrons outside. In quantum electrodynamics, states with positive and negative energies

such as electrons and positrons are described by the same wavefunction; hence, if the electron and positron wavefunctions match each other, there can be transmission through the barrier [31]. In this sense the phenomenon described as Klein tunneling is not a real tunneling effect, since inside the barrier there are some available states for a particle to exist. This is significantly different from the tunneling effect, where a particle has to cross a region with no available states at all. If the barrier is thick enough so that the regular tunnel effect can be excluded, the number of available states in the barrier region is what limits the transmission through it, since a particle needs to find an available state in order to travel into the barrier.

A similar effect can happen in a solid if some of the electrons are within the relativistic regime. In that case, holes take the place of positrons as particles described by states occupying levels with negative energy. The main difference is that in order to generate an electron-hole pair a much smaller energy is needed with respect to the energy of a free electron. In materials with band-touching points, like the topological materials we are interested in, the band gap is zero, and so the electron-hole pairs have zero rest energy. For this reason, every potential barrier has enough energy to hold hole states and the Klein effect manifests itself even for barriers with a low height. If we want to make a device that makes use of a potential barrier we need to take into account of the Klein tunneling and to study its behavior. This does not happen in a regular semiconductor, where electrons and holes are described by separate Schrödinger equations [31].

The Klein tunneling effect has already been observed in Graphene, which presents a similar band structure to the one of topological semimetals, albeit in two dimensions [32]. Some models of Klein tunneling transistor that employ a graphene channel have also been proposed [30, 33], but to our knowledge none have been realized yet, probably due to the difficulty of integrating a single sheet of graphene in a three-dimensional device.

2.2 Field effect devices using Klein tunneling

The idea of the proposed device is to use the gate to produce a potential barrier able to block the carriers, by creating a region where few states are available. Such device could work well for materials where the Fermi level and the Weyl node energy do not coincide, as they would already have many carriers intrinsically and be highly conductive under normal conditions.

Electrons that travel from the source to the drain of the device encounter a potential barrier and are subject to the Klein tunneling. For simplicity, we assume that the barrier generated in this way is perfectly rectangular, but it is possible to adapt the computation to take into account for a smooth energy step, which may be needed to model a real device [34]. This situation is illustrated in Figure 2.1:

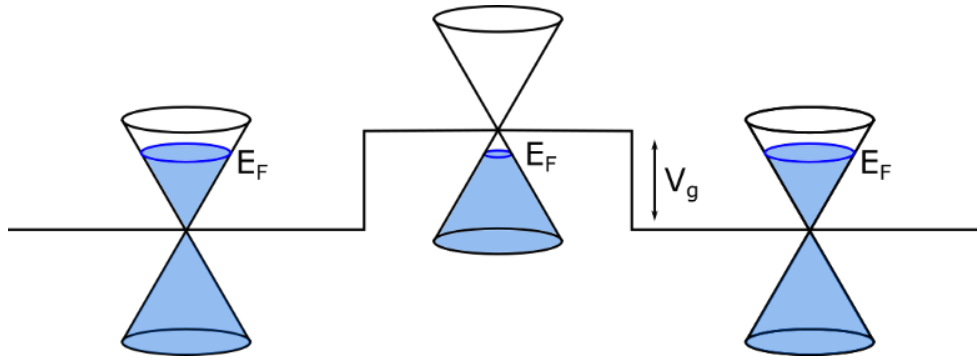


Figure 2.1: Scheme showing the effect of the potential barrier produced by the gate of the device on the band structure of a Weyl semimetal. A single Weyl cone is depicted and the blue volumes represent the occupied states.

As we can see, the effect of the potential barrier is to shift the relative position of the Fermi level with respect to the overall band structure of the material, thus changing the density of available states close to the Fermi level. In Figure 2.1 the available states in the central barrier region are less than in the surrounding ones, so the barrier is able to block a portion of the incoming electrons.

2.2.1 Device geometry

Figure 2.2 shows a scheme of the studied device geometry. It is a fairly simple configuration, formed by a slab of Weyl semimetal that acts as channel, to which the terminals are connected. In our case we assume the bulk, which corresponds to the back gate of the WSM slab, to be connected to ground and we focus on the effect of the gate voltage.

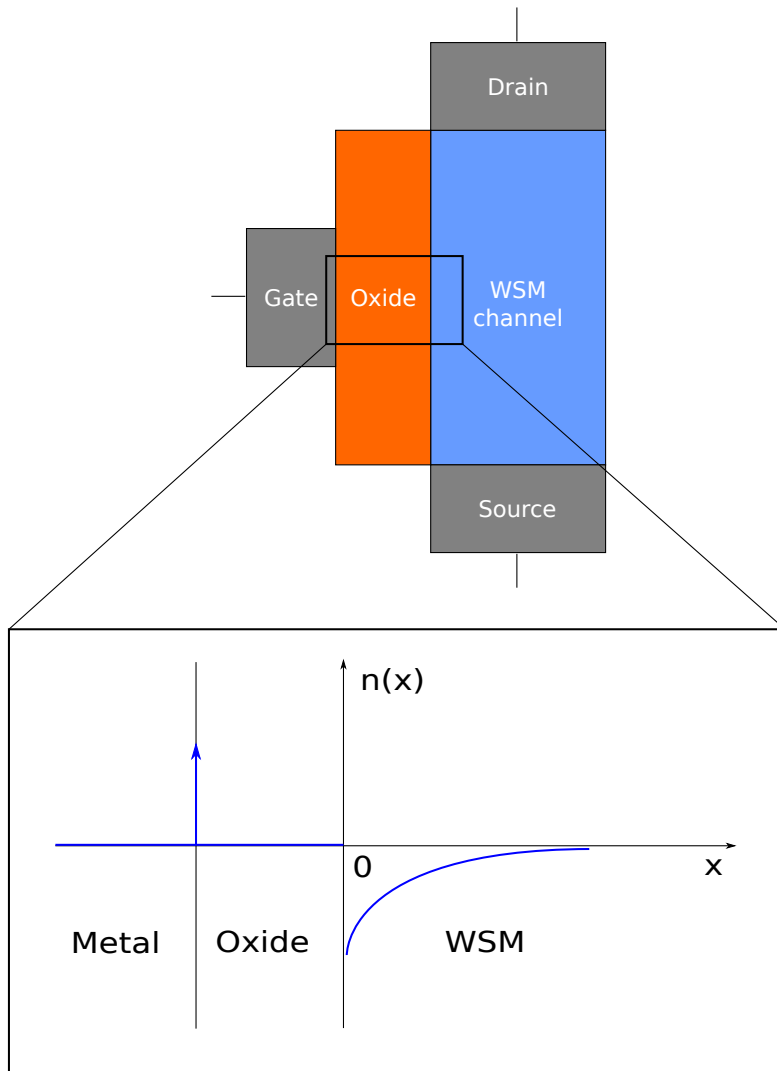


Figure 2.2: Scheme of a Weyl semimetal field effect transistor. Below the device is shown the expected charge concentration when a gate potential is applied. The metal gate is modeled as a perfect conductor, so the charge present in it will be a Dirac delta positioned at its surface, that in the Figure is represented by an arrow.

2.2.2 Scattering against the barrier and critical angle

We can study which carriers are able to propagate their motion inside the barrier region by taking into account the fact that the system is invariant by translation in the two directions parallel to the barrier. Therefore, the parallel momentum components of a particle passing through the barrier interface must be conserved [35]; if this is not possible, the carrier cannot propagate through the interface and is reflected. The following Figure allows to visualize this better, depicting left interface of Figure 2.1, and showing only the range of allowed states with an energy equal to the Fermi level: the states inside the depicted circumferences are the ones that are allowed (the circles are full of states, because the material is three-dimensional and the carriers also have a k_z momentum component that is not shown in the Figure).

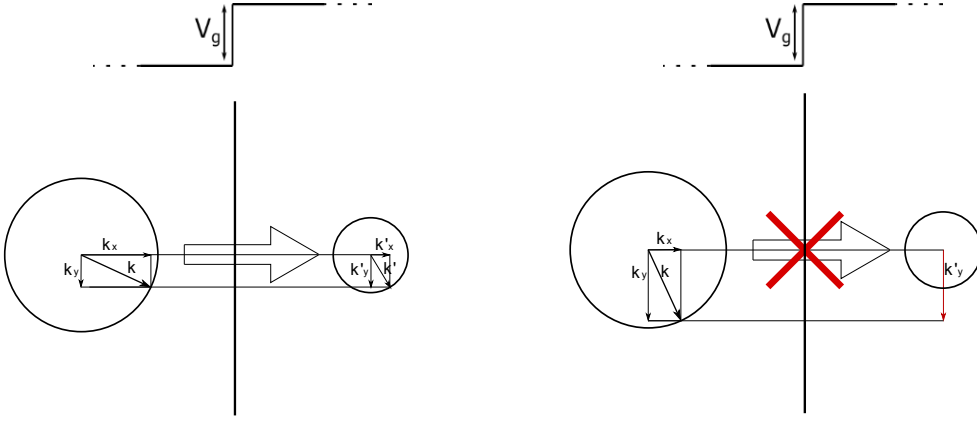


Figure 2.3: Scheme showing the transition of a carrier inside the barrier region. On the left momentum component of the particle parallel to the barrier interface is small enough to allow it to reach a state in the barrier region. On the right, instead, the parallel component of the momentum is too large and the particle is not able to pass trough.

The conservation of the parallel component of the momentum can be written as a function of the incidence angle of the carriers; remembering the linear dispersion relation we can then write the total momentum as a function of the energy, obtaining the following equation, that resembles the Snell's law [35]:

$$E \sin(\theta) = (E - V_g) \sin(\theta') \quad (2.1)$$

where E is the energy of the incoming particle, θ is the angle of incidence, V_g is the height of the barrier and θ' is the refracted angle. We can define a critical angle of incidence, which is the maximum incidence angle that allows the carrier to be transmitted. It is the angle θ that we have when: $\sin(\theta') = 1$. Its expression is the

following:

$$\theta_c = \sin^{-1} \left(\frac{E - V_g}{E} \right) \quad (2.2)$$

This result is displayed in Figure 2.4: the critical angle computed as a function of the barrier height V_g delimits two regions, the inner one in red is characterized by an incidence angle smaller than the critical angle, so the carrier can pass through the interface, while in the white region the opposite situation happens and the carriers are reflected.

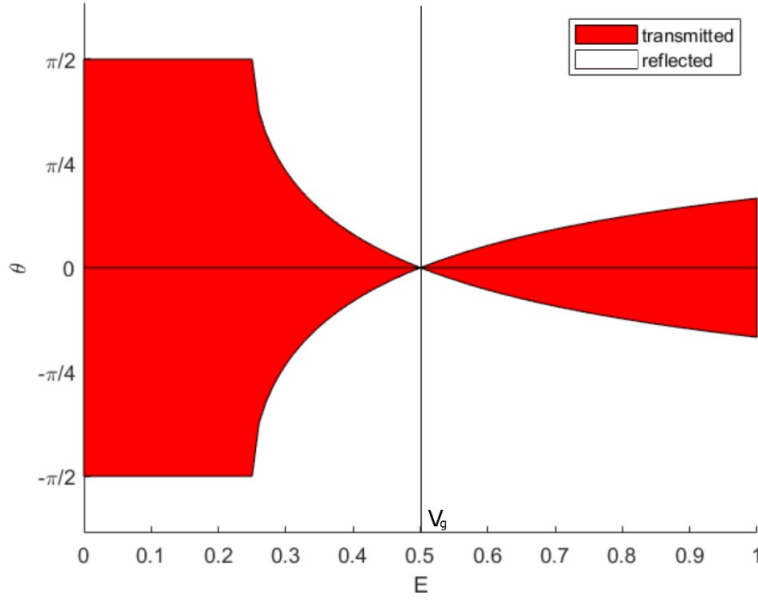


Figure 2.4: Graph showing which carriers are transmitted or reflected at the interface with a potential barrier, depending on their energy and incidence angle.

Considering that the free carriers of the material occupy states with all the available values of the momentum and thus all the possible incidence angles, the total current depends on the number of the carriers close to the Fermi energy that the barrier is able to reflect.

We can also observe another typical characteristic of the Klein tunneling effect that is not found in a regular tunneling process: the barrier is completely transparent for a particle that impinges perpendicularly on it, regardless of the energy of the particle [35]. This is clearly shown in Figure 2.4 and is explained by our considerations on the parallel momentum conservation: a particle with a trajectory that is perpendicular to the barrier has no parallel component of the momentum, and thus will always find an available state inside the barrier, no matter how small the maximum momentum allowed is.

2.2.3 Transmission probability

A more complex model of the device should also take into account the fact that the barrier has a finite length, which may allow some interference phenomena to appear inside it. This situation must be solved by studying directly the wavefunction that describe our carrier. The simplest wavefunction that solves the Weyl equation describing a carrier in our semimetal is a two-component spinor written in the following form [28]:

$$\psi = \begin{bmatrix} \psi_2 \\ \psi_1 \end{bmatrix} = \begin{bmatrix} e^{i\mathbf{k}\cdot\mathbf{r}} \\ \alpha e^{i(\mathbf{k}\cdot\mathbf{r}+\theta)} \end{bmatrix} \quad (2.3)$$

where:

$$\alpha = \frac{|E - V| \sin(\phi)}{E - V + |E - V| \cos(\phi)} \quad (2.4)$$

E is the energy of the particle and V is the value of the potential in a certain region and the angles θ and ϕ define a set of spherical coordinates; we note that to maintain the consistency in our computation we have used z as the propagation direction of the current instead of x , effectively rotating the Cartesian coordinates while keeping the spherical ones in place. As a result, the conversion between the coordinates is the following:

$$\begin{cases} x = -\rho \cos \phi \\ y = \rho \sin \phi \sin \phi \\ z = \rho \sin \phi \cos \phi \end{cases} \quad (2.5)$$

We note that the x and y components of the vector \mathbf{k} are conserved, since they are parallel to the potential barrier. The z component instead, is perpendicular to the barrier and represents the direction along which the macroscopic current of the device propagates. Its value is different in the barrier region with respect to the outside one.

In our system, the particle is described by a linear combination of a forward and a backwards propagating wavefunction of this form [28]. Moreover the value of the potential changes in the middle region, so the parameters of the linear combination must change between the regions, in order to ensure that the wavefunction is continuous. These coefficients represent the amplitude of the wavefunction components inside and outside of the barrier and can provide us the information about the transmission probability through the potential barrier. One way to obtain it is via the transfer matrix approach; the obtained result is the following expression, adapted from [28]:

$$T = \frac{1}{\cos^2(dk'_z) + \sin^2(dk'_z) \left(\tan(\theta) \tan(\theta') - \frac{\alpha}{2\alpha' \cos(\theta) \cos(\theta')} - \frac{\alpha'}{2\alpha \cos(\theta) \cos(\theta')} \right)} \quad (2.6)$$

where d is the thickness of the energy barrier, and k'_z , θ' , ϕ' and α' denote the values of these quantities inside of the potential barrier. These quantities can be computed as usual, but by using the k'_z component inside the barrier, which is:

$$k'_z = \sqrt{|\mathbf{k}'|^2 - k_y^2 - k_x^2} = \sqrt{\left(\frac{E - V}{\hbar v_F}\right)^2 - k_y^2 - k_x^2} \quad (2.7)$$

The obtained transmission probability is plotted in Figure 2.5 as a function of the carrier energy and of the incidence angle θ (ϕ was kept equal to π so that when $\theta = 0$ the particle impinges perpendicularly on the barrier).

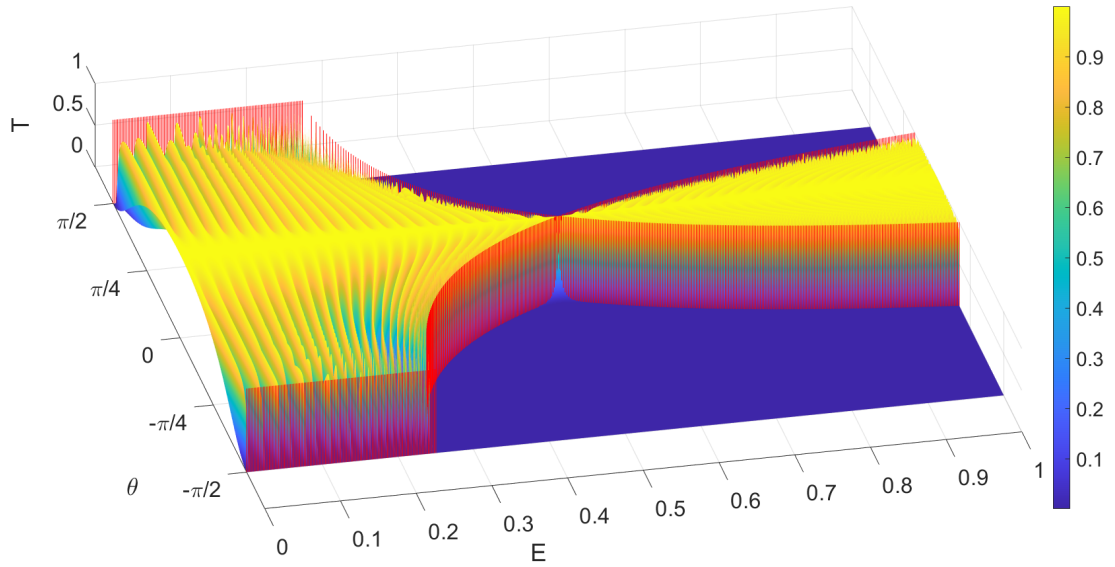


Figure 2.5: Transmission probability of an incoming electron through the potential barrier, as a function of the particle energy E and the incidence angle θ . The height of the potential barrier is $V = 0.5$ eV. The red fencing represents the critical angle, which delimits the region where the transmission probability can be greater than zero.

The red "fencing" that was added on the graph represents some values of the critical angle we computed previously as a function of the energy. As we can see, it perfectly delimits our curve, meaning that this new description is in agreement with the previous considerations.

It is worth noting that this analysis is not completely exhaustive yet, since for now we have always considered states that are all part of the same Weyl cone. Other effects should be taken into account like the scattering between carriers that occupy states in different Weyl cones (the so-called inter-valley scattering) or with

the Fermi Arc states present on the surface of a material. These additional effects are expected to provide contributions to the transmission probability that are much less relevant and can be ignored without committing significant inaccuracies [36].

2.2.4 Current through the potential barrier

The transmission probability can be used to compute the current passing through our potential barrier device. To do so, we assume that some carriers are impinging on the barrier from the forward-propagating states of one electrode of the device, and that the potential barrier reflects some of them. In this case the barrier is the only thing affecting the trajectory of our carriers, so we are in the ballistic transport condition.

Under this assumption, the current flowing in the device can be computed using the Landauer formalism:

$$I = e v_F g(E) T (\mu_L - \mu_R) \quad (2.8)$$

where e is the elementary charge, v_F is the Fermi velocity, which is the propagation velocity of a carrier (it is a constant, since the dispersion relation is linear), $g(E)$ is the bulk density of states described in Equation 3.12, T is the transmission probability through the energy barrier. In this formalism, μ_L and μ_R represent the quasi-Fermi levels of the contacts placed at the sides of the barrier, their difference is used to obtain which carriers can travel from left to right and find a free state to occupy. If we are at a temperature greater than zero this last term should be replaced by the difference of the Fermi-Dirac distributions that describe the occupancy probability of the states in the two electrodes. It is also important to consider the dependence of the transmission probability on the energy and angle of the incoming particles, to keep that into account one must perform an integral over all the possible values of these quantities. The resulting formula is [28]:

$$I = \frac{2eL_xL_y}{\pi\hbar^3v_F^2} \int_{-\infty}^{\infty} \int_{-\pi/2}^{\pi/2} \int_0^{\pi} T [f(E - \mu_L) - f(E - \mu_R)] E^2 \cos(\theta) \sin(\phi) dE d\theta d\phi \quad (2.9)$$

where we already substituted the expression for the bulk density of states of the material. L_x and L_y represent the height and width of the Weyl semimetal channel. Figure 2.6 shows the result of this computation as a function of the height of the potential barrier V_g . In order to obtain this plot, Equation 2.9 was evaluated numerically, as the complex expression of the transmission probability T did not allow for an analytical solution of the integrals.

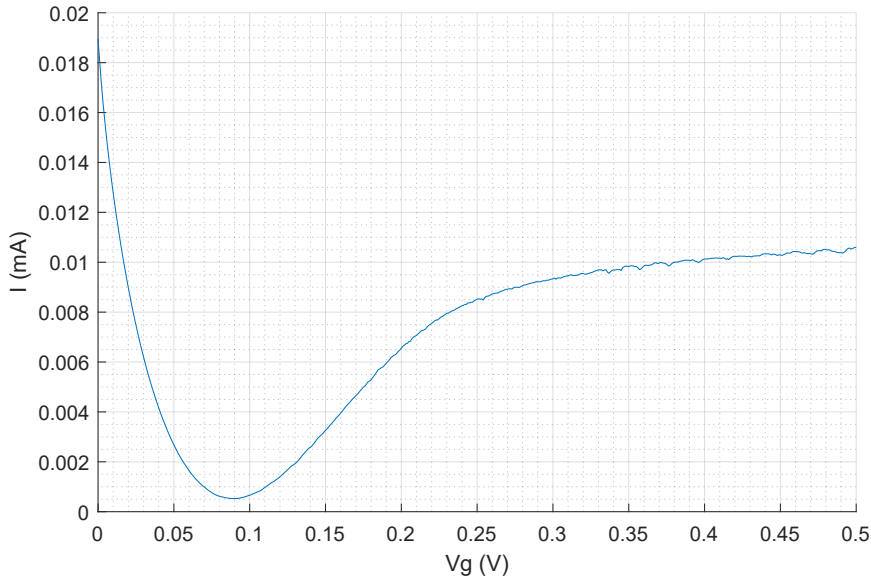


Figure 2.6: Current passing through the potential barrier as a function of the barrier height V_g . This result was obtained from Equation 2.9 using the following parameters: $L_x = 25$ nm, $L_y = 1$ μ m, $V_{DS} = \mu_L - \mu_R = 100$ mV. The thickness of the barrier is $d = 100$ nm.

As we expected from the Klein tunneling effect, the barrier is able to block a significant portion of the current, but not all of it. Moreover, the barrier becomes more and more transparent as its height increases. However, differently from what we have seen before, even if its height reaches very high values, the barrier never returns completely transparent. This is caused by the added oscillations of the transmission probability, which can be seen as the consequence of the Fabry-Pérot resonance of the carriers that find themselves inside the barrier region [37].

The minimum value of the current is obtained when the Weyl node in the barrier region finds itself at the same energy as the incoming carriers, as this means that the carriers reaching the barrier encounter a region where the density of available states is close to zero.

2.3 Screening effect in a Klein tunneling transistor

In the previous section we explained how the current passing through a Weyl semimetal slab can be altered by a potential barrier, that has the effect of reflecting a portion of them, depending on its height. The main aspect missing from this

device model, is that when we try to obtain this effect with a gate electrode, the potential we apply is screened by the material, so the resulting potential barrier has a height that decreases as we move deeper into the the Weyl semimetal slab. In this section we will take into account this effect in our model and study how it influences the behavior of the device.

2.3.1 Voltage profile in the Weyl semimetal channel

As a first approximation, we can expect the applied potential to decay exponentially as we move inside our channel. The rate of decaying is expressed by the screening length which will be a property of the specific material used. However, based on the information provided by the literature, we can estimate the value of the screening length in a Weyl semimetal to be in the order of magnitude of $l_s \simeq 5$ nm [20]. This is a fairly low value, meaning that the material screens well the external fields. The cause for such a good screening is to be found in the fact that the conduction and valence bands of the material touch, allowing it to have many carriers. Moreover, as we have seen, the material presents also some states confined to the surface, which will contribute to the screening.

We can express the height of the energy barrier as a function of the penetration depth x in the following way:

$$V = V_0 \cdot e^{-x/l_s} \quad (2.10)$$

where V_0 will be the height of the barrier at the surface of the Weyl semimetal. We can estimate the value of V_0 , starting from the computation of the electric field, which is related to the derivative of the potential:

$$E = -\frac{\partial V}{\partial x} = \frac{V_0}{l_s} \cdot e^{-x/l_s} \quad (2.11)$$

We also know that the electric field in a capacitor is related to the charge density per unit of surface on its plates. This allows us to compute the electric field in the oxide layer as $E_{ox} = \sigma/\varepsilon_{ox}$. This field will be constant in all of the oxide layer since there are no net charges inside it. This makes it trivial to compute the voltage drop on the oxide:

$$V_{ox} = E_{ox} \cdot t_{ox} = \sigma \cdot t_{ox}/\varepsilon_{ox} \quad (2.12)$$

We can exploit the continuity of the dielectric displacement at the interface between the oxide and the Weyl semimetal to compute the electric field at the surface of the WSM layer:

$$E(0) = E_{ox} \cdot \varepsilon_{ox}/\varepsilon_{WSM} = \sigma/\varepsilon_{WSM} \quad (2.13)$$

This can be used together with Equation 2.11 to estimate V_0 :

$$V_0 = \sigma \cdot l_s/\varepsilon_{WSM} \quad (2.14)$$

The value of V_0 represents the voltage at the surface of the Weyl semimetal, which coincides with the total voltage drop on that layer. The total applied voltage V_g , will be the sum of the voltage dropping on the Weyl semimetal layer and the one dropping on the oxide: $V_g = V_0 + V_{ox}$. It is worth noting that the Weyl semimetal and the metal gate may have different work functions; the difference between them would act as a built-in voltage that is present even when no voltage is applied externally. We do not consider this effect in our computation, since it would only shift the values of the input voltage; if a test device is realized a back gate could be added, to offset this voltage difference. An important consequence of this effect is that it could allow the realization of devices where the applied gate voltage increases the current passing through the device instead of blocking it like in our examples: this would happen if a potential barrier is already present in the device due to the built-in voltage and the applied gate voltage has the effect of reducing its height.

Putting together all the information we have, we can finally obtain the expression of V_0 as a function of the applied voltage V_g , which was needed to write our voltage profile in the material. The final result is:

$$V = V_g \cdot \frac{l_s/\epsilon_{WSM}}{l_s/\epsilon_{WSM} + t_{ox}/\epsilon_{ox}} \cdot e^{-x/l_s} \quad (2.15)$$

We notice that if instead of our Weyl semimetal we had a perfect conductor, with a vanishing screening length, all the voltage would drop on the oxide layer and we would get to the known case of a parallel plate capacitor.

2.3.2 Current computation

In order to compute the current passing through the barrier, we now need to take into account for this change in height that it experiences as a function of the depth x . The barrier height influences the transmission probability therefore, when we compute the current, we need to perform an additional integral to take into account of this new dependence.

This computation becomes challenging for the computer to perform, since we are now integrating four times over a function, the transmission probability, that has some rapid oscillations and this computation has to be repeated for each point of our graph. In order to reduce the computation time, we implemented an algorithm that uses a lookup-table approach: the current is computed first and for all the values of the barrier height that we need. This is similar to what we have done in Figure 2.6, but this time we no longer multiply for the thickness of the channel L_x : the current computed in this way can be seen as the current density of a two-dimensional slice of the channel. Then, we can compute the total current as

the sum of the currents densities of many slices, each of them multiplied by a vanishing slice thickness.

The advantage of this method is that we were able to replace one integral with a sum, which is much faster to compute. Moreover we can now perform the computation of the integrals only once for each input value, store it in the memory of our computer and use it when needed. Instead, with the four nested integrals computation the internal integrals were instead solved many times with the same inputs, causing a lot of redundancy.

The main disadvantage is that with this approach we have more possible sources of error in our computation than with a regular integral, like the fact that the barrier height must be present in the set of values we are pre-computing, and the fact that the thickness of the slices can be small but not infinitesimal as it should be in theory. Moreover the numerical integration methods in MATLAB usually allow to set a maximum value of the computation error on the final result, while this method does not. In order to check that the results obtained with this approach are still correct, we tuned the parameters used, like the thickness of the slices, until the results converged to a fixed value, and then we confronted them with a previous computation made with the four nested integrals approach: in this case the results were the same, but the computation time with the lookup table approach was much faster.

Figure 2.7 shows an example of the results of this computation:

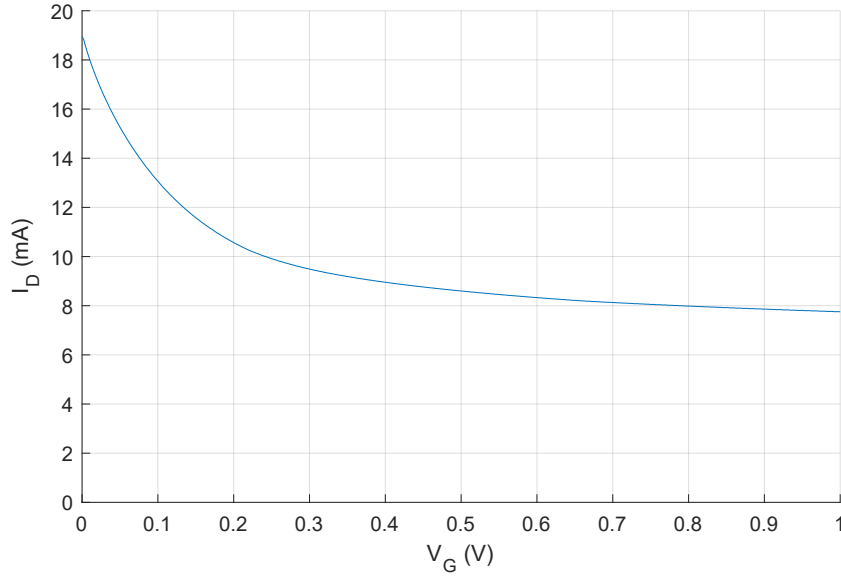


Figure 2.7: Current passing through the device as a function of the applied gate voltage V_g . To obtain it we used the following parameters: $L_x = 25$ nm, $L_y = 1$ μ m, $V_{DS} = \mu_L - \mu_R = 100$ mV. The length of the barrier region encountered by the carriers is $d = 100$ nm.

We notice that a good portion of the current is still able to pass through the channel, even when the potential barrier is active. This is likely due to the fact that the barrier is present only in the region of the channel that is closest to the surface, while the rest of it remains unaffected.

We can see this in more detail by performing the same computation with different values of the channel thickness, as shown in Figure 2.8:

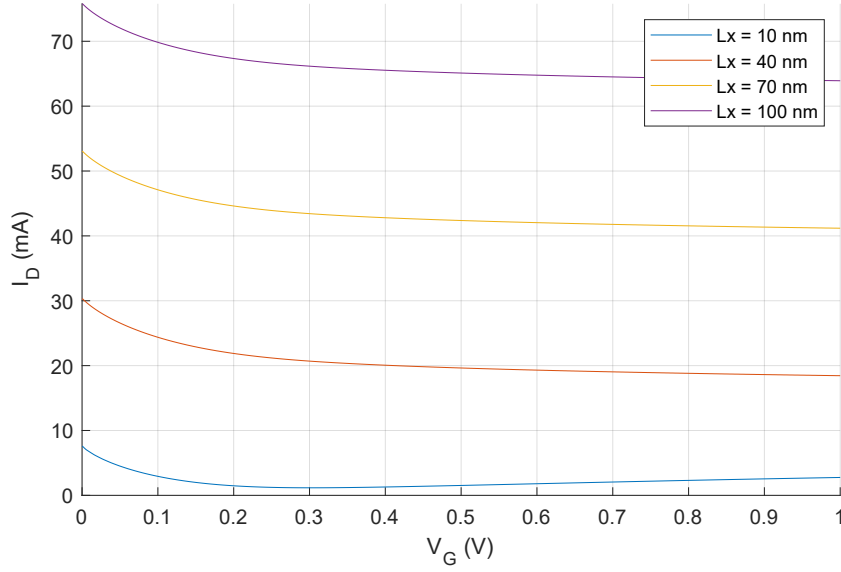


Figure 2.8: Current passing through the device as a function of the applied gate voltage V_g , for different values of the channel thickness. For this computation we used the same parameters as in the previous figure.

As we can see from this plot, as the gate thickness is increased, the total current passing through it increases, however the current modulation due to the effect of the gate saturates, as all the curves except the lowest one have almost the same trend. This confirms our description of the phenomenon, where the potential barrier is created only close to the surface of the material, while the rest remains unaffected.

The fact that the current is not completely blocked in the off-state of the transistor is not a big issue, since these devices target high-frequency applications, where a constant current is easy to filter out. Instead, the fact that the screening effect is limiting the modulation of the signal can be an issue, as it reduces the overall gain. We can estimate the gain of a transistor as the derivative of the output current with respect to the input gate voltage, this quantity is called trans-conductance: $g_m = \partial I / \partial V_g$. Figure 2.9 shows the trans-conductance of the transistor obtained from each of the previous curves:

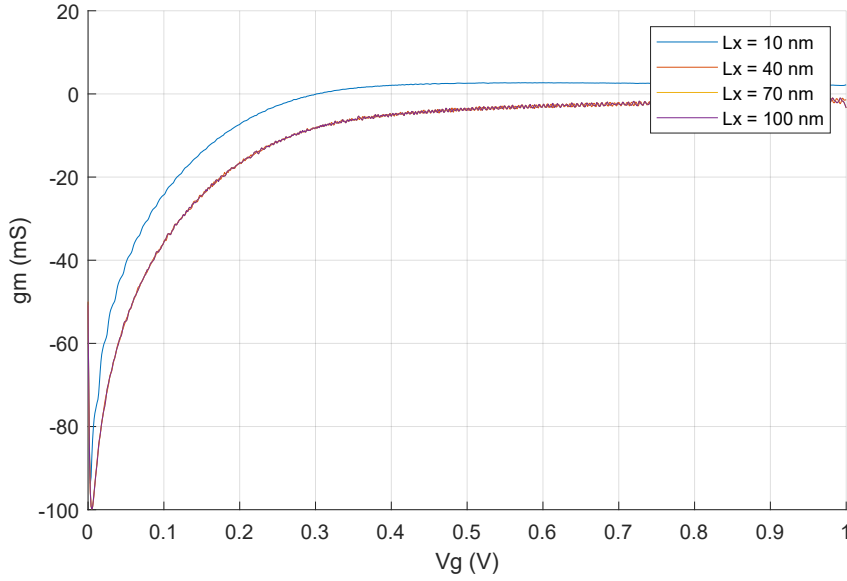


Figure 2.9: Trans-conductance of the device as a function of the applied voltage, for different values of the channel thickness.

The gain of this kind of device tends to saturate as the applied potential increases. Moreover, all of the curves except for the first one are exactly the same. This is in agreement with our idea that the barrier is screened after a distance of the order of three or four times l_s , affecting only a small portion of the channel. As a result the performance of the device is dominated by the screening effect and by the thickness of the region coupled to the gate. We will now study what happens when we change the value of the screening length, which in this model is the parameter that tunes the decaying depth of the potential. The results are shown in Figure 2.10:

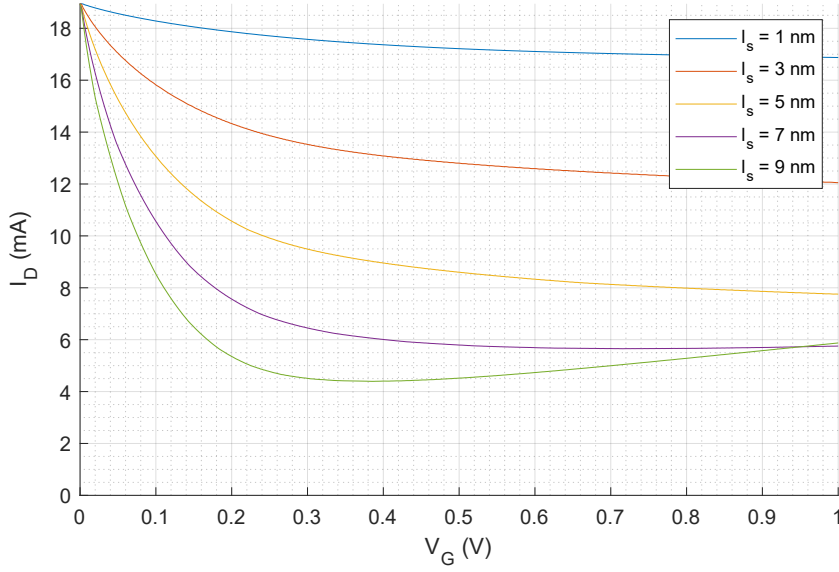


Figure 2.10: Current in the transistor channel as a function of the applied voltage, for different values of the screening length. The channel thickness used is 25 nm.

As we can see the modulation of the current is affected by the screening length and, as a consequence, so is the gain. For this reason, the properties of the material, and in particular its carrier density and its ability to screen the external fields are of particular interest in the description of a field effect device.

In the next chapter we will study more deeply the screening effect in a type-I Weyl semimetal, to better understand the extent of the region affected by the gate of the device, and how it changes depending on the temperature and on some material parameters. We already know, however, that a thin channel is preferred for the device to work properly, as the regions of it that are far away from the surface are difficult to control.

Further work is needed in order to make a complete model of the device, as some additional effects may alter its behavior: some topological materials, when deposited as a thin film, present a band structure with a small band-gap, which is due to confinement effects [38, 39]. This phenomenon could be useful for the device, as it would create an energy range with no available states, thus increasing the reflectivity of the potential barrier. On the other side however, this would also mean that the bands are no longer linear, so the mobility of the carriers could be reduced. Moreover, the models about Klein tunneling in topological semimetals available in the literature do not take into account the fact that the carriers in the Fermi Arc surface states also provide a contribution to the channel current. This contribution may become more relevant as the thickness of the film is reduced.

Chapter 3

Screening in Weyl semimetals

In this section we will study how an external potential is screened in a Weyl semimetal, in order to improve our description of the field effect in this class of materials. The goal is to make a better model of field effect devices that use a Weyl semimetal channel, to estimate the modulation of the charge inside the channel in response to the potential applied.

The literature on this subject was less comprehensive than on the Klein tunneling effect studied previously, so the work had to start from the definition of the physical problem we are considering, with the description of the material properties and the geometry of the system. In this chapter, we start by describing the results found in the literature, that we used as a base for our work, then we move to the description of the problem and finally we solve it, showing the obtained results.

3.1 Previous works on screening

The most relevant studies on the screening effect found in literature cover the effects of the bulk and surface densities of states of a Weyl semimetal, at zero Kelvin and for materials where the Fermi level coincides with the energy of the Weyl nodes. Under these conditions it is possible to directly integrate the density of states in the bulk to obtain the following screening equation [40]:

$$U''(x) = \frac{4ge^2}{3\pi(\hbar v_F)^3} U^3(x) \quad (3.1)$$

The solution to this equation is of the type $U(x) \propto 1/x$. This result is unexpected, as such a function would have a tail that decays much slower than the exponential

function used in common screening models [41]. A similar approach was used with respect to the Fermi Arc states, obtaining the following equation [20]:

$$U''(s) = g \left(\int_{-1}^1 du (1 - u^2) e^{s(u^2-1)} \right) U(s) \quad (3.2)$$

where $s = x (\Delta k/2)^2 / m v_F$ represents a re-scaling of the spacial coordinate x . In this case the solution is similar to an exponential function, where the exponent changes as a function of the position in space, due to the fact that the effect of the surface states is reduced as we move far away from the surface. The solution of this equation was compared to the previous one, showing that, always in the case of $T = 0$ K and $E_F = 0$ eV, the effect of the surface states is generally stronger than the one of the bulk, except when particularly high fields are applied [20].

The work of this thesis tries to provide a more comprehensive study of the screening effect, taking into account the contributions of both types of states at the same time, as well as providing a more detailed theoretical basis for our computation. The resulting model could be used to predict the behavior of a field effect device under more realistic conditions.

3.2 Material model

For our model we consider an ideal type-I Weyl semimetal, in which the only bands close to the Fermi level are the topological ones, that feature a couple of Weyl nodes. The reason for this is that the presence of trivial bands near the Fermi level will cause the material to have carriers that do not present the properties typical of Weyl fermions. We also take into account the set of topological surface states associated to our couple of Weyl nodes. To further simplify the computation we assume our Weyl nodes not to be tilted, so that the Fermi velocity is the same along the three spacial directions ($v_{Fx} = v_{Fy} = v_{Fz}$).

These limitations could be easily lifted in order to adapt the model to a specific material. For example if a material had four degenerate Weyl nodes instead of two, like the case of Ag_2S [13], one could simply change the degeneracy factor by which the density of states of a Weyl cone (Equation 1.6) is multiplied (this parameter will be later called g). If the Weyl nodes of the material instead are at different energies, one would need to consider the densities of states of the different bands separately and consider the fact that a shift in energy must be added to take into account for the different positions of the Weyl nodes. Figure 3.1 shows a simplified scheme of the band structure used:

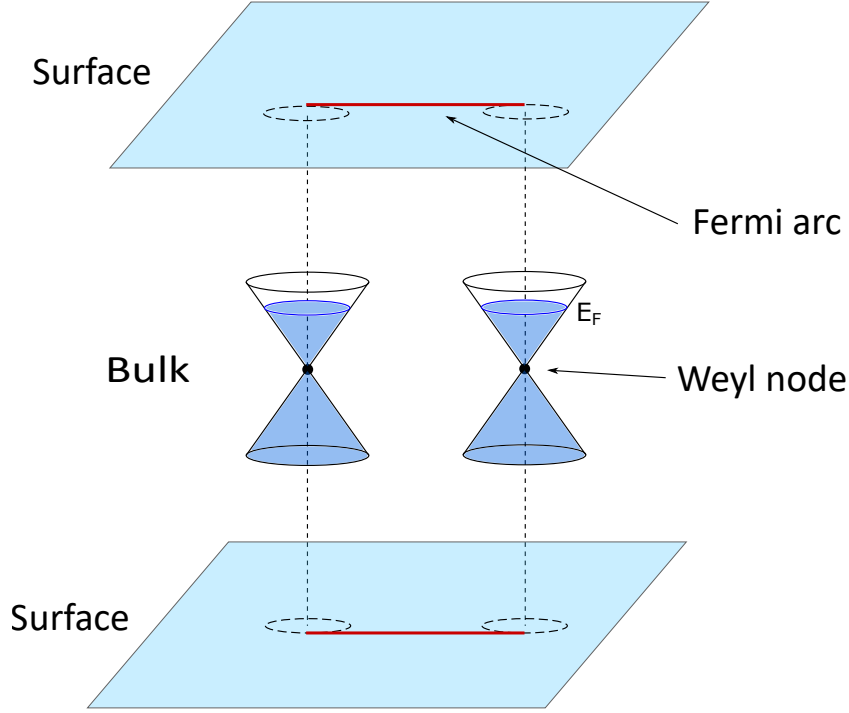


Figure 3.1: Simplified scheme of a Weyl semimetal band structure used for the screening model.

The bands used as a model for our computations are described by the Hamiltonian in Equation 1.7, using the following parameters, that are taken from [20].

$$\begin{aligned}\Delta k &= 1 \text{ nm}^{-1} \\ m &= 5 \text{ eV}^{-1} \text{ nm}^{-2} \\ \hbar v_F &= 0.25 \text{ eV nm}\end{aligned}$$

They refer to Na_3Bi , a material that can present multiple topological phases, including the type-I Weyl semimetal [42].

3.3 Physical approach

We can start our computation with the expression of the density of carriers present in our material:

$$n = \int_{-\infty}^{+\infty} \frac{D(E)}{1 + \exp\left\{\frac{E-\mu}{k_B T}\right\}} dE \quad (3.3)$$

This formula is obtained by performing an integral over the energy of the density of states $D(E)$ of our material, weighted by the Fermi-Dirac distribution function,

that expresses the probability of occupancy of each state depending on its energy. In this equation μ represents the chemical potential inside the solid, its value will in general depend on the temperature and on the Fermi energy of the material. If the temperature is zero, the chemical potential will be by definition equal to the Fermi energy.

The total electrical potential present in a certain point of our solid will alter the density of carriers locally. This effect can be modeled as a shift in the value of the energy of the carriers:

$$E(\mathbf{k})' = E(\mathbf{k}) - eU(\mathbf{r}) = \hbar v_F |\mathbf{k}| - eU(\mathbf{r}) \quad (3.4)$$

This is correct only if the the potential varies slowly in space, so that an electron feels the effect of a constant value of potential [41]. For this to happen, the potential must vary slower than the scale of the space occupied by an electron, which corresponds to the size of its wave packet. If instead the hypothesis is not satisfied, the electrons will not be able to fully follow the potential variation, and the charge density in one point will no longer depend only on the value of the potential in that position.

Since the states we are considering are located in a small region centered in a Weyl node of the material in momentum space, we can approximate the electronic wave vector to the one of the Weyl node, which will be half the distance Δk between the two Weyl nodes of the same couple, or alternatively, half the length of a Fermi Arc. With the material parameters used, we have $1/\Delta k \simeq 1$ nm. As we will see in Section 3.7, the charge density tends to vary slower with respect to this length, meaning that our hypothesis is reasonable.

We can then take into account the effect of the local potential in the expression of the carrier density in the following way:

$$n(\mathbf{r}) = \int_{-\infty}^{+\infty} \frac{D(E)}{1 + \exp\left\{\frac{E - eU(\mathbf{r}) - \mu}{k_B T}\right\}} dE \quad (3.5)$$

From this equation the effect of the electrical potential can be also seen as a local shift of the chemical potential of the material ($\mu'(\mathbf{r}) = \mu + eU(\mathbf{r})$).

If we assume that the material is neutral at the equilibrium condition, we can compute the charge density inside it by taking the difference between the carrier density that we obtain with the potential applied and the one we would have at equilibrium, all multiplied by the charge of the electron:

$$\rho^{ind}(\mathbf{r}) = -e [n(U(\mathbf{r})) - n(0)] \quad (3.6)$$

This equation is at the basis of the Thomas-Fermi theory [41]. Because of the neutrality assumption, the only charge imbalance present in our material will be

due to the effect of the potential. We can then link this charge density to the potential intensity by using the Poisson's equation:

$$U''(x) = -\frac{1}{\varepsilon} \rho^{ind}(x, U(x)) \quad (3.7)$$

We write this equation only along the x axis, because the problem we are solving is one-dimensional, as the potential difference that we will have in our structure will be between the gate and the channel, thus always perpendicular to the interfaces between the different materials. This differential equation is what we need to solve to obtain our results.

An important parameter present in the Poisson equation is the relative permittivity of the material. Its role is to take into account the fact that the electrons are not in vacuum, and the ions of the crystal add an additional contribution to the screening of the potential. This effect will be more significant the fewer free carriers are present in the material, to the point where it becomes the only contribution if the material is an ideal insulator.

For this reason we can write $\varepsilon = \varepsilon_0 \cdot \varepsilon_{lattice}$ where $\varepsilon_{lattice}$ is the relative permittivity of the ionic lattice.

3.3.1 Lattice permittivity

In order to provide a value for the relative permittivity of the crystal lattice we use the information provided by [43], which presents a model that well describes the behavior of oxides and other materials that do not experience conductive mechanisms. In fact, we can imagine our crystal lattice to behave similarly to an oxide if the conductance electrons are not taken into account.

Based on this model we can compute the dielectric polarizability of a compound as the linear combination of the individual polarizabilities of the ions that compose it:

$$\alpha = \sum_{i=1}^N n(i) \alpha_D(i) \quad (3.8)$$

where $\alpha_D(i)$ is the polarizability of a certain ion, and $n(i)$ is the number of times that ion appears in the unit cell of the material. The ion polarizabilities were obtained by fitting the values of total polarizability of some known materials [43]. The values we are interested in are $\alpha_D(Na) = 1.8 \text{ \AA}^3$ and $\alpha_D(Bi) = 6.12 \text{ \AA}^3$. From them we obtain:

$$\alpha(Na_3Bi) = 3 \alpha_D(Na) + \alpha_D(Bi) = 11.52 \text{ \AA}^3 \quad (3.9)$$

We can then use the dielectric polarizability of the material to compute its relative permittivity, by using the Clausius-Mosotti equation:

$$\varepsilon_{lattice} = \frac{3V_m + 8\pi\alpha}{3V_m - 4\pi\alpha} \quad (3.10)$$

where V_m is the volume of an unit cell of the material. We can compute V_m by taking the molar volume of the material [44] and diving it by the Avogadro number; this results in $V_m \simeq 125 \text{ \AA}^3$. Substituting into Equation 3.10 we finally obtain our result:

$$\varepsilon_{lattice} \simeq 3 \quad (3.11)$$

3.4 Surface and bulk charge densities

In this Section we will compute the expression of the total charge density as a function of the local potential, which is needed to solve the Poisson's equation. Since in our model we are considering two main types of states, the bulk Weyl fermions and the Fermi Arcs, the charge density will be a sum of the contribution of the two: $\rho = \rho_{bulk} + \rho_{surface}$. We can compute them both starting from the respective densities of states.

3.4.1 Bulk states

Knowing that the dispersion relation of a Weyl fermion is $E = \hbar v_F k$, and that we are in a three-dimensional system, we can easily obtain the density of states in the bulk of our material:

$$D(E)_{bulk} = \frac{g}{\pi^2 v_F^3} E^2 \quad (3.12)$$

where v_F is the Fermi velocity and g is the number of degenerate Weyl nodes. As we discussed in Section 3.2, this expression is an approximation valid only in the proximity of the Weyl nodes, for a material where no trivial bands are present in the considered energy interval.

We can use Equation 3.5 to compute the carrier density, but in our case, the integral would diverge for $E \rightarrow -\infty$. This is due to the fact that the expression for the density of states is defined only in a small energy interval, and does not possess a lower bound. However, for our model we do not need to know the total number of electrons in the solid, but only its variation from the equilibrium condition. We can then consider as a reference the number of states with energy lower than the Weyl node energy, which will correspond to the density of electrons present in an ideal material at zero temperature. We can call this number n_w . In a generic sample the density of electrons will be obtained by adding to this number the number of states occupied at a higher energy with respect to the Weyl node (which are analogous to conductance electrons in a semiconductor) and subtracting the states that are empty and at a lower energy (which are analogous to holes). This corresponds to

the following computation:

$$\left\{ \begin{array}{l} n(U(x)) = n_w + n'(U(x)) - p'(U(x)) \\ n'(U(x)) = \frac{g}{\pi^2 v_F^3} \int_0^{+\infty} \frac{E^2}{1 + \exp\left(\frac{E - \mu - eU(x)}{k_B T}\right)} dE \\ p'(U(x)) = \frac{g}{\pi^2 v_F^3} \int_{-\infty}^0 \frac{E^2}{1 + \exp\left(\frac{\mu + eU(x) - E}{k_B T}\right)} dE \end{array} \right. \quad (3.13)$$

The charge density that is induced in the bulk by the effect of the applied potential, will be proportional to the difference between the carrier density when the potential is applied and the one we would have at equilibrium:

$$\rho_{bulk}^{ind}(x) = -e [n(U(x)) - n(0)] = -e [(n'(U(x)) - n'(0)) - (p'(U(x)) - p'(0))] \quad (3.14)$$

As expected the constant term n_w that we defined has no impact on the computation of this quantity.

At this point the expression of the charge density can be used to solve the Poisson equation. One could perform a Taylor expansion of the functions $n'(U)$ and $p'(U)$, in order to simplify the computation; in this case however, we decided to keep them as they are, since the differential equation that we have to solve will require a numerical solution in any case.

3.4.2 Chemical potential

In order to compute the obtained expressions, we still have to evaluate the chemical potential in our solid. This can be done by imposing that the number of electrons in our solid must be constant at all temperatures, and that the chemical potential is equal to the Fermi energy when we are at zero Kelvin. This information allows us to write:

$$n_w - p'(\mu(T, E_F)) + n'(\mu(T, E_F)) = n_w + \frac{g}{\pi^2 v_F^3} \frac{E_F^3}{3} \quad (3.15)$$

where on the left side we computed the total number of electrons in the solid at a finite temperature and on the right side we computed the same number at $T = 0$ K. The solution of this equation allows us to compute the chemical potential for every value of temperature and Fermi energy.

In the current computation we are only taking into account the bulk states, since in a three-dimensional solid we can expect the number of states available in

the bulk to be much greater than the one in the surface, so the effect of the surface states should be negligible. Allowing electrons to migrate from the surface into the bulk would also mean that our solid is no longer neutral as we assumed.

Since the top and bottom part of the Weyl cones in our model are symmetrical, if the Fermi level is at zero energy, also the chemical potential will be, and it will not move if the temperature is changed. Instead if the Fermi level is not zero, the chemical potential will necessarily be located between it and the Weyl node.

3.4.3 Fermi Arc states

From the Fermi Arc wavefunction shown in Equation 1.8 we can compute the density of states of the Fermi Arcs. The result is the following [20]:

$$D(E)_{surface} = \frac{g/2}{(2\pi)^2 v_F} \int_{-\Delta k/2}^{\Delta k/2} \frac{(\Delta k/2)^2 - k_z^2}{mv_F} e^{\frac{k_z^2 - (\Delta k/2)^2}{mv_F} x} dk_z \quad (3.16)$$

This equation contains an integral over the z component of the momentum, which is performed to include the contributions of all the states present in the Fermi arc. This integral, however, does not have a closed form solution and this is the reason why most of our computations are performed numerically. We can also notice that this density of states is constant with the energy. This greatly simplifies our computation as it can be taken out of the integral:

$$n(U(x)) = D(E)_{surface} \int_{-\infty}^{+\infty} \frac{1}{1 + \exp\left(\frac{E - \mu - eU(x)}{k_B T}\right)} dE \quad (3.17)$$

As a result the value of temperature and Fermi energy will have no effect on the response of the electric charge on the potential intensity. We can better show this by solving the integral and computing the expression of the charge density. In fact, we notice that now we have to integrate the Fermi Dirac distribution alone, which can be done analytically, allowing us to write:

$$n(U(x)) = D(E)_{surface} \left[E - \mu - eU(z) - k_B T \ln \left(1 + e^{\frac{E - \mu - eU(z)}{k_B T}} \right) \right]_{-\infty}^{+\infty} \quad (3.18)$$

As before we can use Equation 3.6 to compute the charge induced at the surface of the material:

$$\begin{aligned} \rho_{surface}^{ind}(U(x)) &= -e(n(U(x)) - n(0)) \\ &= D(E)_{surface} \left[e^2 U(x) + ek_B T \ln \left(\frac{1 + e^{\frac{E - \mu - eU(x)}{k_B T}}}{1 + e^{\frac{E - \mu}{k_B T}}} \right) \right]_{-\infty}^{+\infty} \\ &= D(E)_{surface} (e^2 U(x) + 0) \end{aligned} \quad (3.19)$$

As expected the term depending on temperature and Fermi energy of the material cancels out. The charge density of the Fermi Arc states will then be:

$$\rho_{surface}^{ind}(x) = e^2 D(E)_{surface} U(x) \quad (3.20)$$

The fact that the density of states of the Fermi Arcs is constant with the energy is reasonable as many two-dimensional systems present this property. However in this case it is likely to be the effect of the approximation of our model.

3.5 Boundary Conditions

In order to study the effect of the screening in our material, we would need to solve the Poisson equation, which is a second order differential equation. To do so two boundary conditions are needed; these can be obtained by studying the geometry of our system. Since we are applying a known potential on a metal gate, this potential will partially drop on the Weyl semimetal channel and partially on the oxide layer that connects them. With this information, we are already able to draw the qualitative behavior of the charge density, the electric field and the electric potential in our system.

With this information, we can obtain the boundary conditions required to solve our problem. We can start by imposing that the gate potential must be the sum of the voltage drops on the oxide and on the WSM layers. We assumed to have a reference ground connection on the other side of the WSM layer, so that the voltage drop on the WSM will be equal to the electric potential found at the surface of the WSM that is in contacts of the oxide. Using the same coordinate system as in Figure 3.2, we can write this as $U(0)$: this quantity is one of the initial conditions necessary to find our solution.

In order to compute the voltage drop on the oxide, we can exploit the fact that this layer contains no mobile charges and is overall neutral. This means that the electric field inside it will be constant and, as a result, the electric potential can simply be computed as:

$$V_{ox} = E_{ox} \cdot t_{ox} \quad (3.21)$$

where t_{ox} is the thickness of the oxide layer. We also know that the dielectric displacement must be continuous at the interface between the oxide and the Weyl semimetal, which yields the relation:

$$E_{ox} = E(0^-) = E(0^+) \cdot \varepsilon_{lattice} / \varepsilon_{ox} \quad (3.22)$$

For the WSM layer we used the lattice permittivity, since the screening due to the conduction electrons is taken into account separately by considering the charge induced in proximity of the interface.

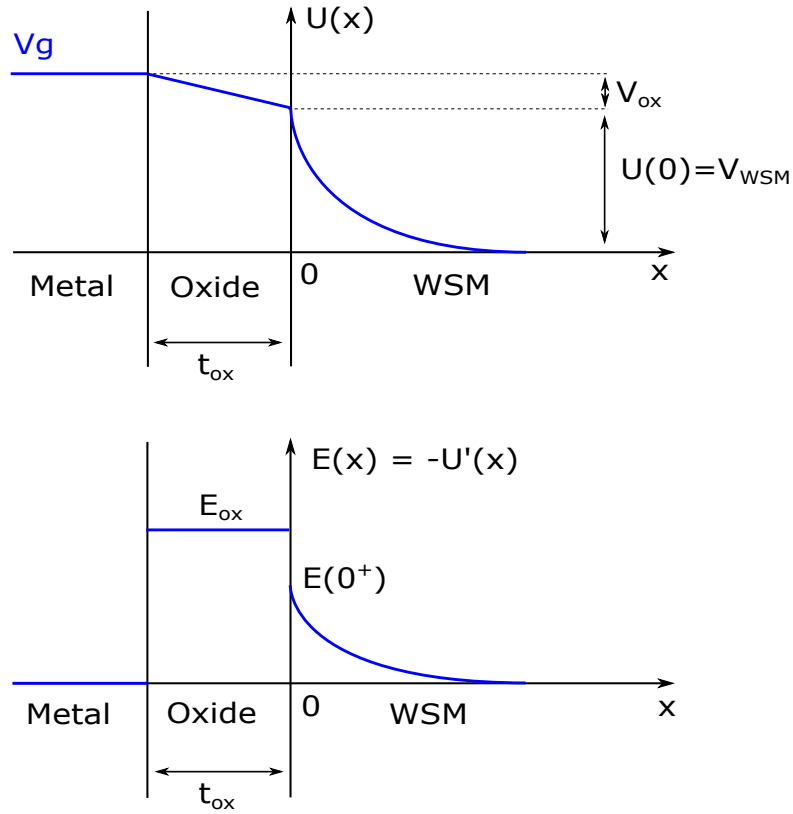


Figure 3.2: Qualitative graphs of the electric potential $U(x)$ and of the electric field $E(x)$ in the proposed device. The graphs display only the direction we are interested in, which is along a section perpendicular to the interfaces that separate the three materials.

$E(0^+)$ represents the electric field at the surface of the WSM, and by its definition we can write $E(0^+) = -U'(0^+)$ which explicitly shows the connection to the electric potential. Since the electric potential is the solution of our differential equation, the electric field that represents its derivative is also one of the quantities we need as initial conditions to our problem. By substituting each equation into the previous one, we obtain:

$$V_g = U(0) - U'(0^+) \cdot t_{ox} \cdot \varepsilon_{lattice} / \varepsilon_{ox} \quad (3.23)$$

A second condition that our solution must satisfy is that the potential must be zero at the end of the WSM channel, as this position coincides with the ground connection:

$$U(x = \text{WSM thickness}) = 0 \quad (3.24)$$

Notice that the two conditions we found are specified in two different points of space, that have the peculiarity of being the extremes of the interval where the solution function is defined. This is called a *Boundary Value Problem*.

3.6 Solution of the Poisson equation

Differently from the regular *Initial Value Problems*, having two boundary conditions does not guarantee that the solution exists or that it is unique. The fact that the two boundary conditions are not set in the same point makes the solution of the differential equation more challenging. We were able to overcome this issue first by implementing an iterative algorithm that called a regular Initial Value Problem solver many times, and afterwards by using the Boundary Value Problem solver implemented in Matlab.

More information on how the two approaches work can be found in Appendix A.

3.7 Results

We can finally show the results of our computation; starting with the most ideal conditions and then gradually moving away from them to study the effect of the different physical parameters.

3.7.1 Ideal conditions

We start by studying the system at $T = 0$ K and $E_F = 0$ eV. The Poisson differential equation is solved numerically with an applied gate voltage of $V_G = 0.1$ V.

For our computation we used the following device dimensions: the thickness of the oxide layer is 100 nm and the thickness of the Weyl semimetal channel is

200 nm. These dimensions should be fairly easy to obtain when trying to realize a similar device. The area of the device is does not influence the computation.

The results are shown in Figure 3.3:

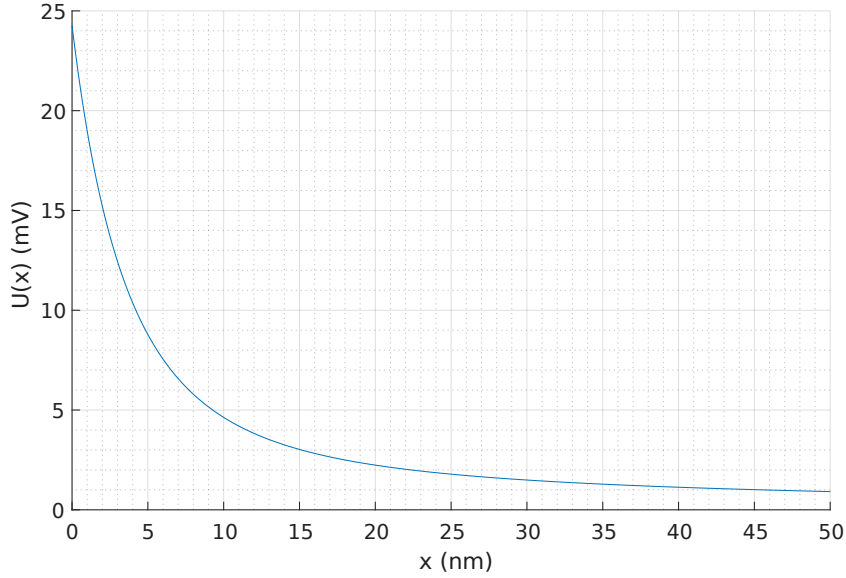


Figure 3.3: Total potential profile as a function of the depth inside the material at $T = 0$ K and when the Fermi level coincides with the Weyl node energy ($E_F = 0$ eV). The voltage applied is $V_G = 0.1$ V.

Note that in the graph only the region of the Weyl semimetal slab closer to the oxide is shown, as in the rest of it the potential is negligible. We are however imposing that the potential should be zero only at the end of the slab.

This graph provides us some preliminary information on the behaviour of the studied material. From this, we already notice that the screening effect is quite strong as the effect of the potential is greatly reduced just a few tens of nanometers away from the surface. We also notice that most of the potential applied on the gate is dropping on the oxide layer rather than on the Weyl semimetal. This can be easily seen by the fact that the potential at the surface is a small portion of the total one on the gate.

Once the potential profile is known, it can be used to compute the other quantities used in our equations. In particular we are interested in the charge density that is induced in our material. This can be done in two ways: either by using the Poisson equation (Eq. 3.7) or with the definition of the charge density (Eq. 3.6). The second way is the best, as it allows to separate the contributions of the bulk and surface states. It is also worth noting that since a numerical computation was performed, taking the second derivative of a function, as required by the Poisson

equation, would mean to perform the finite differences of its points, which could introduce noise and significantly degrade the result. Figure 3.4 shows the charge density induced in the material in the same conditions used above:

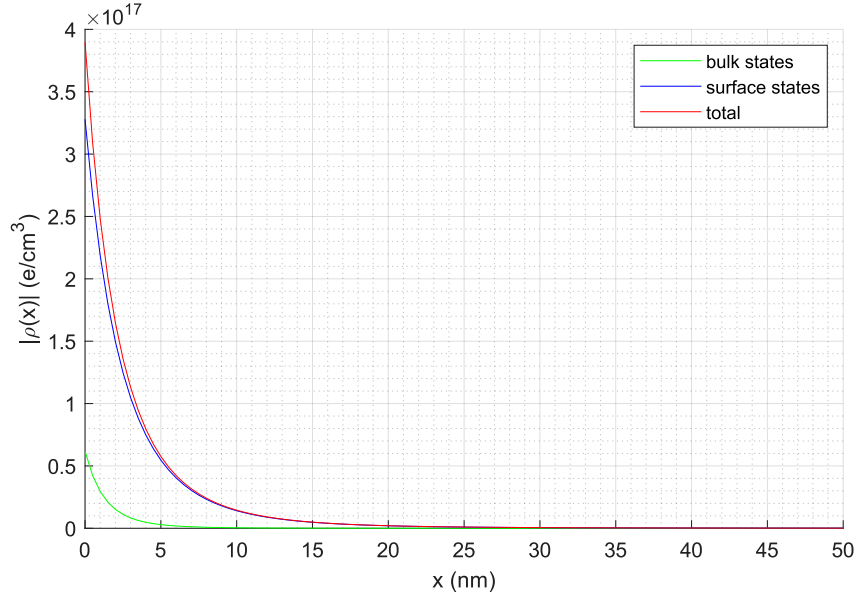


Figure 3.4: Charge density as a function of the depth inside the material at $T = 0$ K and $E_F = 0$ eV. The green and blue curve represent the surface and bulk contributions respectively, while the red curve is the sum of the two. The voltage applied is $V_G = 0.1$ V.

Under these conditions most of the charge induced in the material resides in the surface states, and their contribution to the screening is the dominant one. The contribution of the bulk states becomes more and more relevant if the gate potential is increased. An example of this is shown in Figure 3.5, obtained with the same parameters as before, but with a gate voltage of $V_G = 0.3$ V.

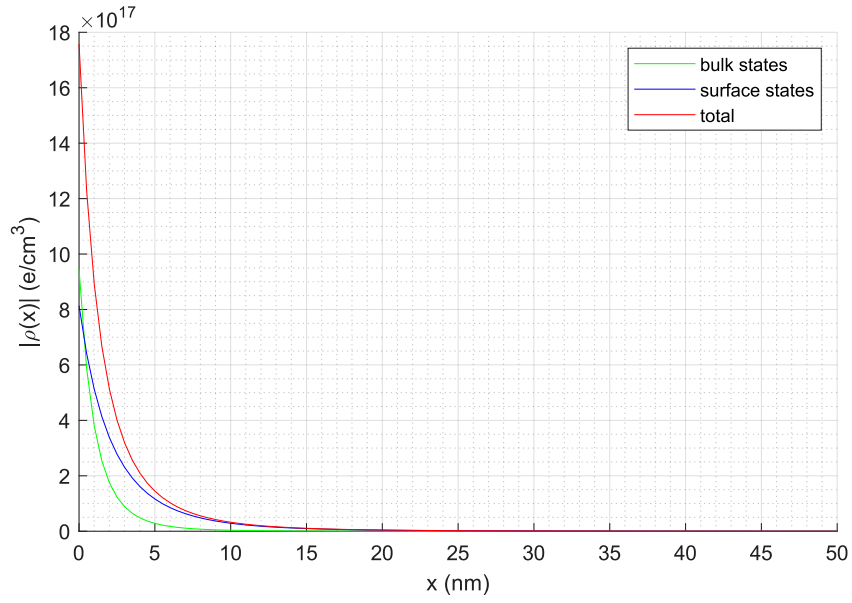


Figure 3.5: Charge density as a function of the depth inside the material at $T = 0\text{ K}$ and $E_F = 0\text{ eV}$. The green and blue curve represent the surface and bulk contributions respectively, while the red curve is the sum of the two. The voltage applied is $V_G = 0.3\text{ V}$.

This is in agreement with the literature [20] and can be explained by the fact that the response of the bulk states increases as the third power of the potential, as shown by equation 3.1. We can also study the two contributions separately by considering only one kind of state at a time. Figure 3.6 shows the decay of the potential in a material under the same conditions as before but where only the bulk states are present.

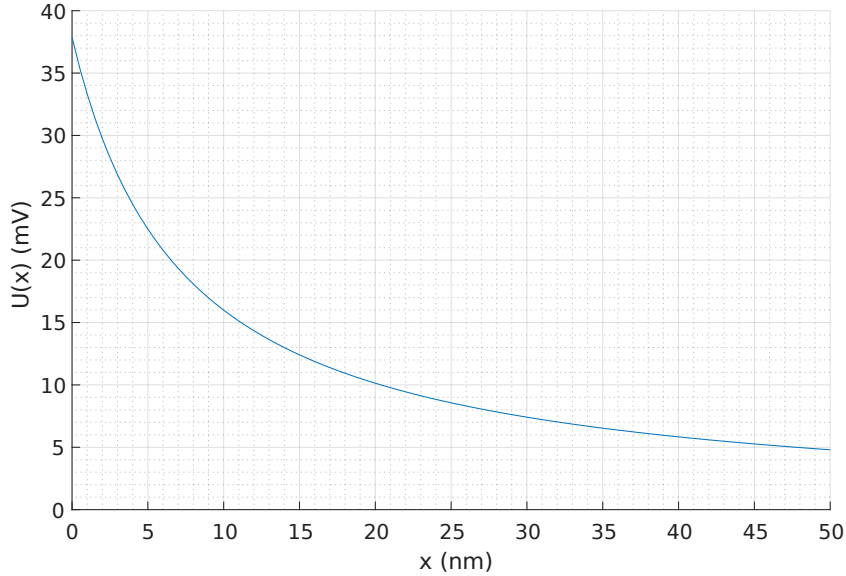


Figure 3.6: Total potential profile as a function of the depth inside the material at $T = 0$ K and when the Fermi level coincides with the Weyl node energy ($E_F = 0$ eV). Only the effect of the bulk states is taken into account. The voltage applied is $V_G = 0.1$ V.

We notice that by removing the dominant contribution, which is the one of the surface states, the screening effect is much weaker and, also a greater portion of the applied potential drops on the Weyl semimetal layer. The potential profile in this case can be well fitted with a function of the kind $f(x) = a/(x + b)$ as expected from the previous studies [40] (the values obtained are $a = 0.26$ and $b = 6.77$ and the fit has a coefficient of determination $R^2 = 0.992$, this means that the fit is particularly good). The parameter a is related to the physical constants present in the screening equation, while b does not have a direct physical meaning, but it is necessary to avoid a vertical asymptote of the solution at the interface, which would be non-physical, therefore allowed by the boundary conditions we have set.

This behavior of the potential profile is peculiar and is likely due to the fact that there are currently no available states at the Fermi level. In particular this means that the potential has a very long tail and lingers for a long distance inside

the material. This effect is likely to be overcome by other contributions to the screening, like we have seen when the effect of the surface states was considered.

3.7.2 Effect of the Fermi level

An important parameter in describing the electronic properties of the material is the position of the Fermi level of the material with respect to the Weyl nodes. In an ideal case they should be exactly at the same energy, however, the presence of charged impurities in the crystal may change the position of the Fermi level similarly to what happens in a semiconductor. It is also worth noting that some Weyl semimetals like TaAs present multiple Weyl nodes that are located at different energies [12], so they will intrinsically present some bands where the energy of the Weyl node does not coincide with the Fermi level.

In this case, the Fermi level will find itself in a region of the bands where the density of states is finite, so the results will be different than what we saw in the previous section. As we showed in Section 3.4, only the bulk density of states will be affected by this, as the Fermi Arc one is constant in our model.

In this analysis we use the energy shift between the Fermi level and the Weyl nodes as an independent parameter. This property however, is not so easy to tune when dealing with an actual material. In the case where the shift is due only to atomic impurities, we can compute the Fermi level as a function of the concentration of impurities by computing the number of electronic states that must be occupied or freed in order to maintain charge neutrality:

$$n_i = \frac{g}{\pi^2 v_F^3} \frac{E_F^3}{3} \quad (3.25)$$

This computation allows to obtain the Fermi energy shift as a function of the density of atom impurities n_i .

We can start by considering the screening due to the bulk states only, and how it is affected by the Fermi level position; the results obtained are shown in Figure 3.7. The Fermi level energy is expressed with respect to the one of the Weyl nodes, the maximum energy difference considered is $E_F = 0.05$ eV which corresponds to the energy at which the two Weyl cones of our material will merge together, and the bands will have a saddle point. If we move further away from the Weyl nodes our description of the density of states will no longer be accurate.

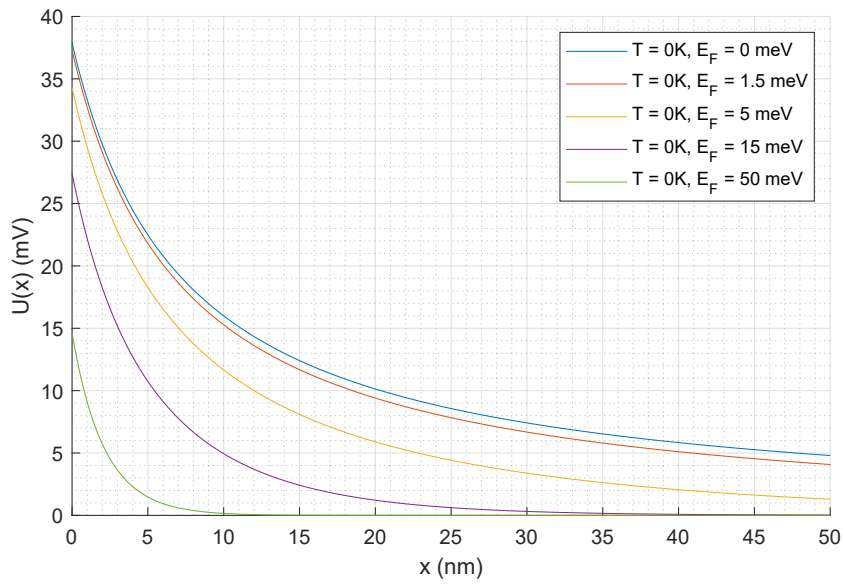


Figure 3.7: Total potential profile as a function of the depth inside the material at $T = 0\text{K}$ for various values of the Fermi level. Only the effect of the bulk states is taken into account. The voltage applied is $V_G = 0.1\text{V}$.

We can see that the screening of the external potential becomes significantly stronger as a result of the shift in energy of the Fermi level. We also notice that the potential curve changes shape from the $1/x$ we had before to an exponential decay. This can be shown by performing a fit of the curves obtained: the one with $E_F = 0$ was performed in the previous section; if instead we fit the curve with the highest value of the Fermi energy ($E_F = 50$ meV) with an exponential function of the form $f(x) = a \cdot e^{b \cdot x}$ we get a perfect fit (as shown in Figure 3.8).

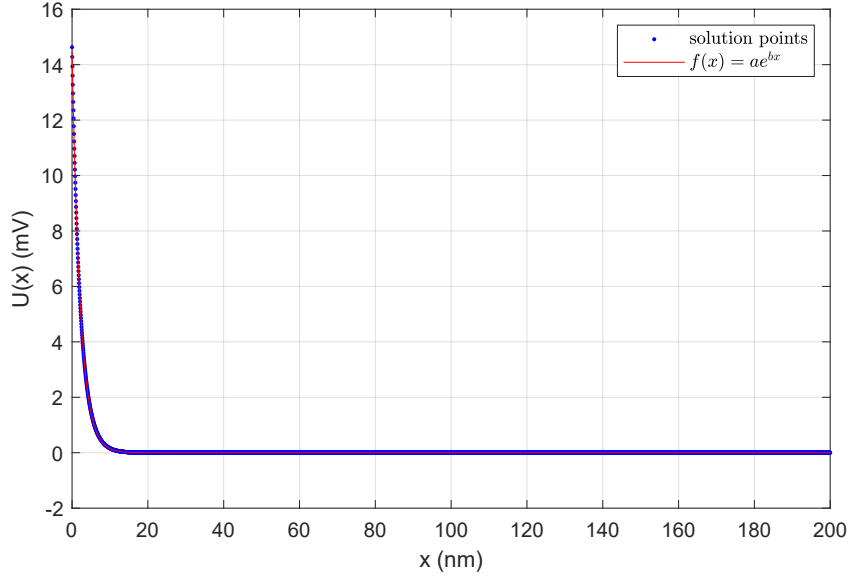


Figure 3.8: Fit of the last solution (green curve) of Figure 3.7 with an exponential function. The whole thickness of the Weyl semimetal slab, where the function is defined is shown. The resulting fit parameters are $a \simeq 1.5 \cdot 10^2$, $b \simeq -0.46$ and $R^2 = 0.9999$.

This result can also be explained by the theory: if we tried to obtain something similar to Equation 3.1 by integrating the bulk density of states where the energy is shifted by the Fermi level ($D(E)_{bulk} = g/\pi^2 v_F^3 (E - E_F)^2$) we would obtain an equation of the following type:

$$U''(x) = \frac{4ge^2}{\pi(\hbar v_F)^3} \left(\frac{U^3(x)}{3} + U^2(x)E_F + U(x)E_F^2 \right) \quad (3.26)$$

In this case if the Fermi level is large enough the term of the equation that is linear would tend to dominate, and the resulting solution would be an exponential function, as we experienced in the simulation.

After these considerations, we can reintroduce the effect of the surface states

and use our model to study what would happen in the actual material. This can be seen in Figure 3.9.

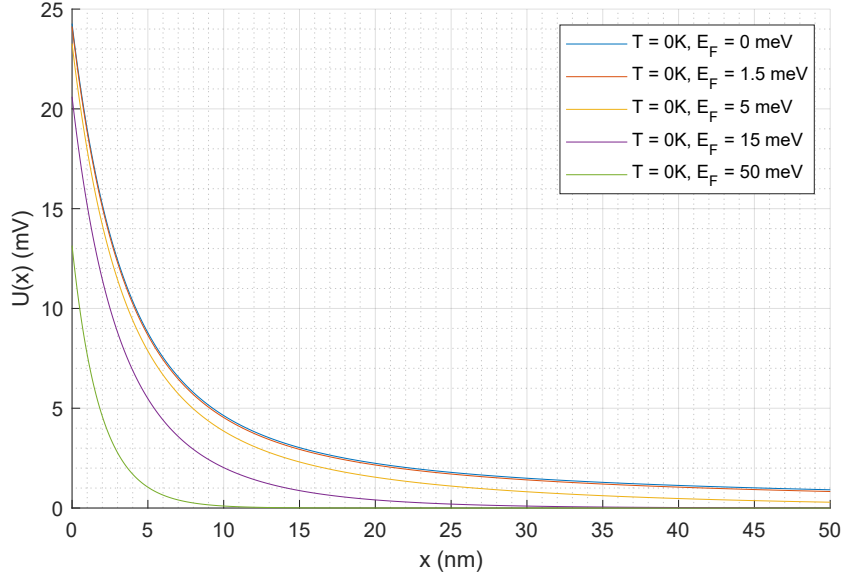


Figure 3.9: Total potential profile as a function of the depth inside the material at $T = 0$ K for various values of the Fermi level. The voltage applied is $V_G = 0.1$ V.

By confronting this plot with Figures 3.3 and 3.8 we can conclude that the effect of the surface states remains always significant for the screening under the conditions of our study, but that the bulk states acquire more and more importance as the Fermi level is moved away from the position of the Weyl node, since the number of free carriers in the bulk tends to increase.

3.7.3 Effect of the Temperature

We can now repeat our computation by changing the temperature of the system, in order to study its effect. As before, we can expect the temperature to act only on the bulk states and leave the surface unaffected, however it is harder to predict how strong will this change be, as it manifests as a weighting of the density of states that is integrated. In Figure 3.10 we show the total potential as a function of the depth in the material for different values of the temperature, while keeping the Fermi energy to zero. Our model also allows us to study what happens when both the temperature and the Fermi level are different than zero, as shown in Figure 3.11.

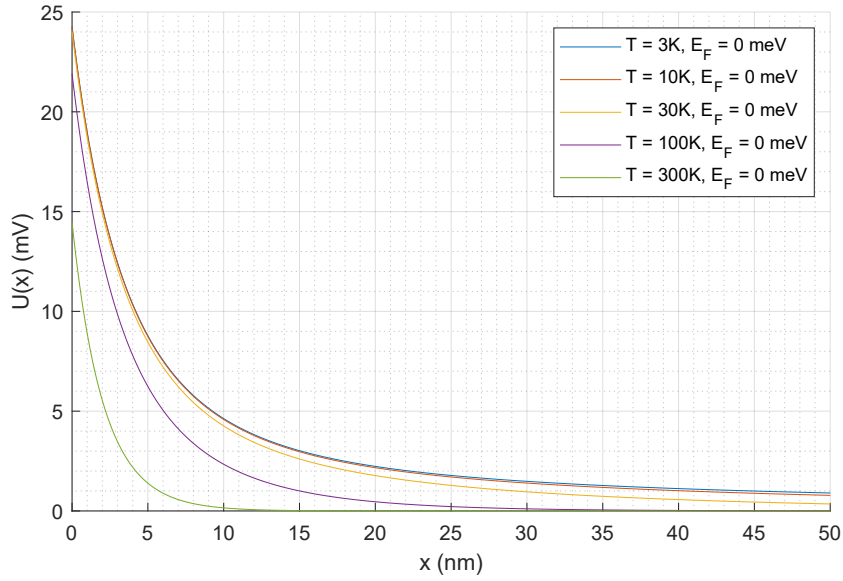


Figure 3.10: Total potential profile as a function of the depth inside the material for different values of the Temperature. The Fermi level has been kept fixed to the Weyl node energy. The voltage applied is $V_G = 0.1$ V.

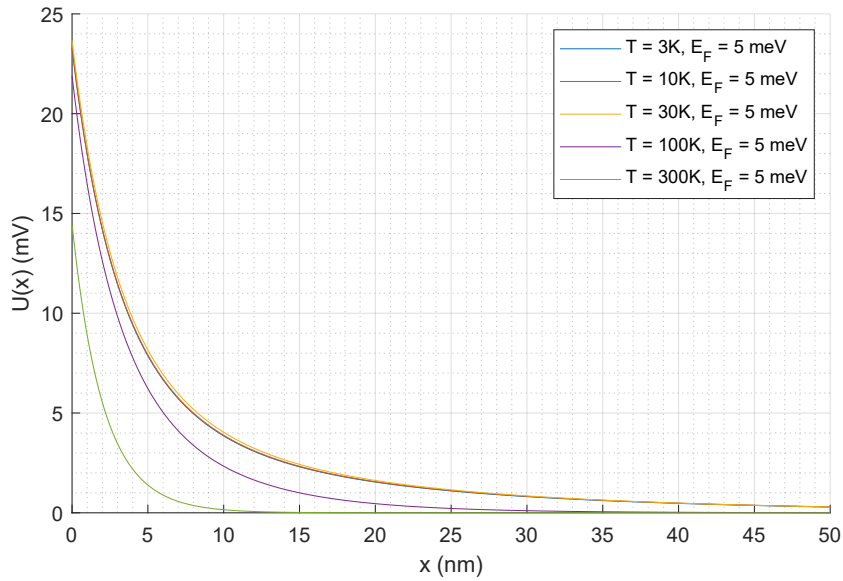


Figure 3.11: Total potential profile as a function of the depth inside the material for different values of the Temperature. The Fermi level has been kept fixed to 5 meV. The voltage applied is $V_G = 0.1$ V.

It is worth noting that if the Fermi energy is different from zero, the temperature will also have the effect of modifying the the chemical potential, bringing it closer to the Weyl node. For this reason Figure 3.11 is different from the previous one only in the curves obtained at low temperatures.

3.7.4 Effect of the distance between the Weyl nodes

Another important material parameter is the distance between two coupled Weyl nodes Δk . Its value can change when an external magnetic field is applied.

If Δk is increased the length of the Fermi Arcs increases and, as a result, they are able to host more states. In Figures 3.12 and 3.13 we show how this affects the screening: as we can expect if the length of the Fermi Arcs is increased the screening will be stronger. We are also able to see how the charge induced in the material tends to reside more in the layer close to the surface and less in the bulk of the material.

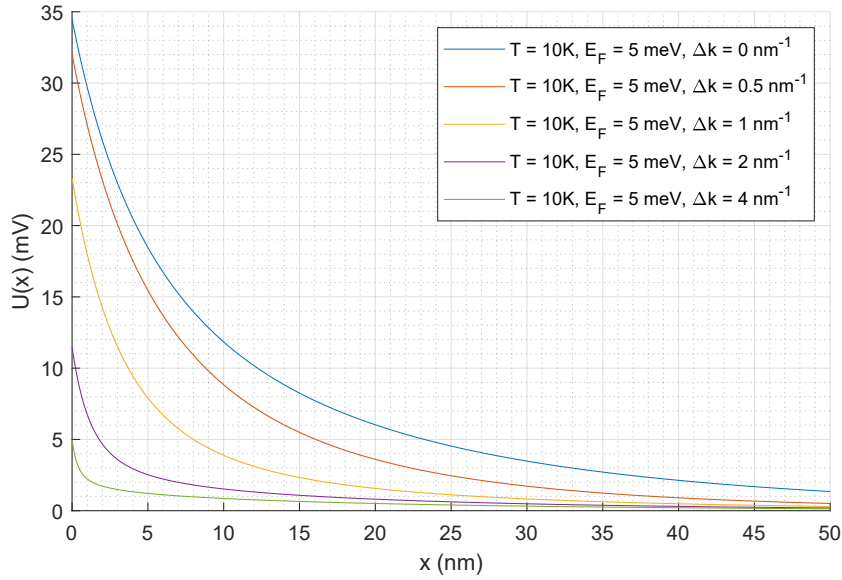


Figure 3.12: Total potential profile as a function of the depth inside the material for different values of the separation in momentum space between the Weyl nodes. The voltage applied is $V_G = 0.1$ V.

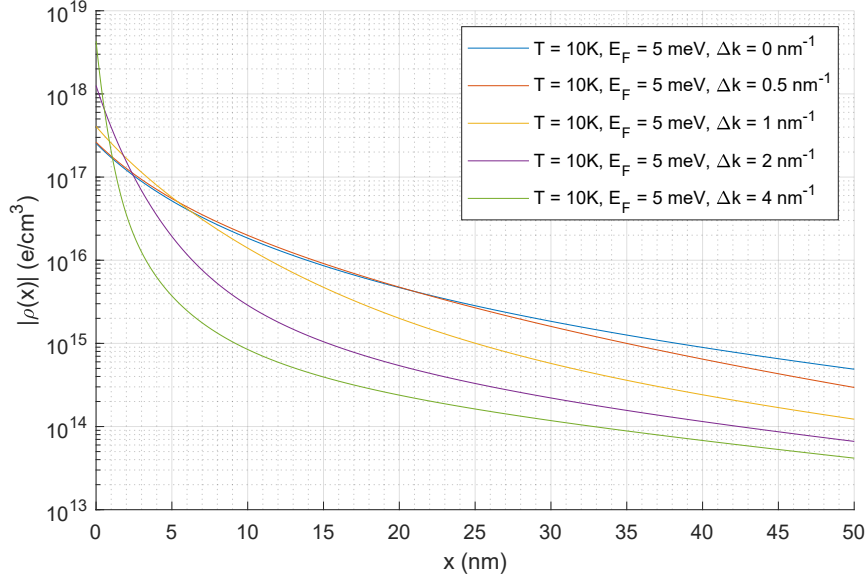


Figure 3.13: Charge density as a function of the depth inside the material for different values of the separation in momentum space between the Weyl nodes. The voltage applied is $V_G = 0.1$ V.

3.7.5 Gate capacitance computation

The information we obtained on the charge density can be used to compute the gate capacitance of our structure. This can be achieved by simply using the definition of capacitance:

$$C = \frac{\partial Q}{\partial V} \quad (3.27)$$

Since we have not specified the area of the gate contact, it is easier to normalize the capacitance per unit area. To perform our computation we then need to compute the charge accumulated in our channel per unit area, which can be done by integrating the charge density over the penetration depth: $Q = \int_0^{Lx} \rho(x) dx$. The derivative with respect to the gate voltage can be computed numerically using the finite differences method. The resulting computation is the following:

$$C = \frac{Q(V_G + \delta V_G) - Q(V_G)}{\delta V_G} = \frac{\int_0^{Lx} \rho(x, V_G + \delta V_G) dx - \int_0^{Lx} \rho(x, V_G) dx}{\delta V_G} \quad (3.28)$$

The results are shown in Figure 3.14:

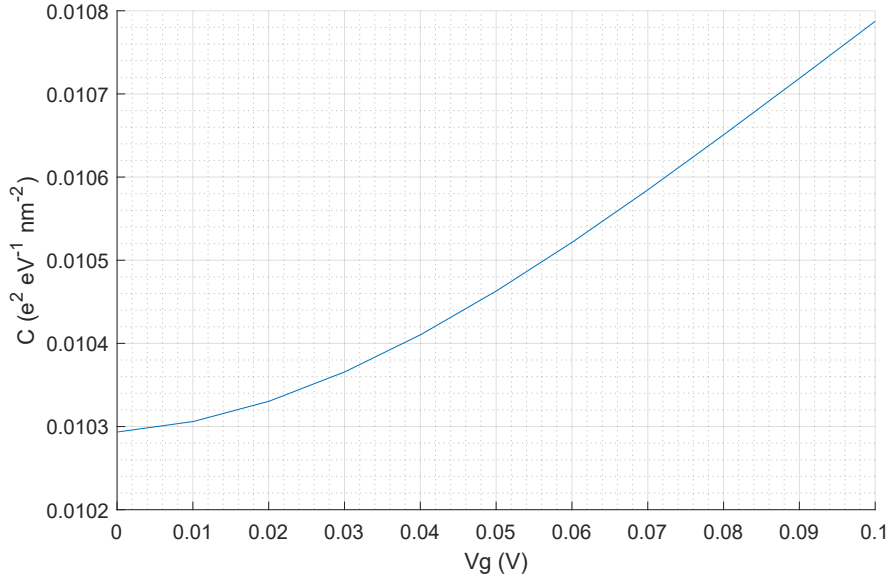


Figure 3.14: Gate capacitance per unit area as a function of the voltage applied. Obtained with $E_F = 0$ eV and $T = 10$ K.

From this graph we see that the capacitance increases slightly with the applied gate voltage. The obtained value of the capacitance per unit area is around $C \simeq 0.0105 e^2 eV^{-1} nm^{-2}$.

The gate capacitance can be modeled by two capacitors connected in series: the capacitance due to the parallel plate capacitor (where the gate and the Weyl semimetal are the plates) and a second component due to the finite density of carriers present in the Weyl semimetal (called quantum capacitance). The role of this component is to take into account that, due to the finite density of states, not all the charge in the Weyl semimetal resides exactly at the interface. For this reason the total capacitance is reduced, and this reduction is greater the fewer carriers are available. If instead of the Weyl semimetal we had a perfect conductor, the only relevant term would be the parallel plates capacitor and the result in that case would be:

$$C_{parallel\ plates} = \frac{\epsilon_0 \epsilon_{ox}}{t_{ox}} \simeq 0.0138 \frac{e^2}{eV\ nm^2} \simeq 2.2 \times 10^{-7} F/cm^2 \quad (3.29)$$

Which as expected is slightly above what we obtained with our computation.

We can then repeat the same computation with $T = 300$ K. Under these conditions the material should have more free carriers than before, so the capacitance should be higher, while still remaining lower than the parallel plate case. This is exactly what happens, as we obtain $C \simeq 0.0118 e^2 eV^{-1} nm^{-2}$.

3.7.6 Applications of the screening model

The screening model described in this work allows us to better understand the physical properties of Weyl semimetals and their interaction with electric fields. In addition, it can be used to build a model of a device, and study its performance. As an example, we can use it to provide a more accurate description of the Klein tunneling transistor that we studied in the previous chapter. We can do so by replacing the exponential profile of the potential we used before, with the one computed by solving the Poisson differential equation. The results are shown in Figures 3.15 and 3.16 where we computed the current and trans-conductance as a function of the applied gate voltage for different values of the temperature of the system.

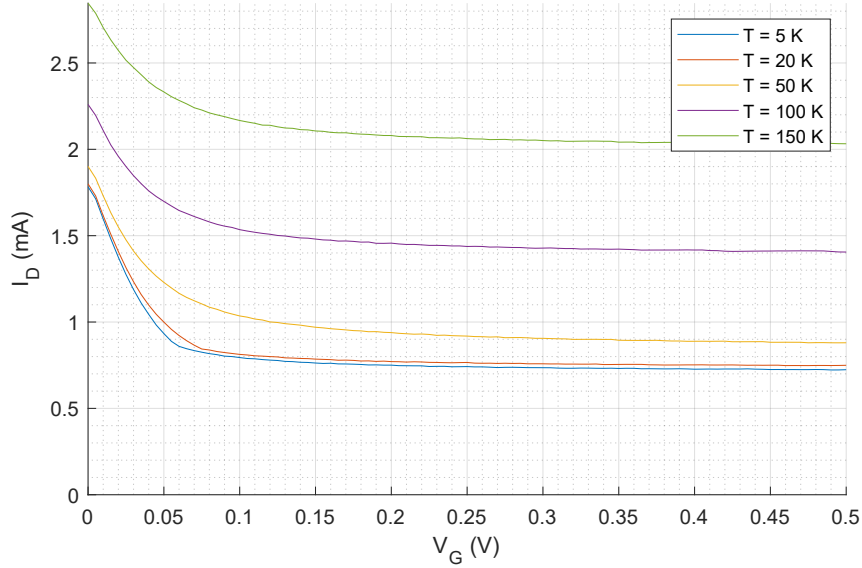


Figure 3.15: Current passing through the Klein tunneling transistor as a function of the gate voltage applied, for different values of the temperature. The following parameters were used: $V_{DS} = 50$ meV, channel thickness = 30 nm.

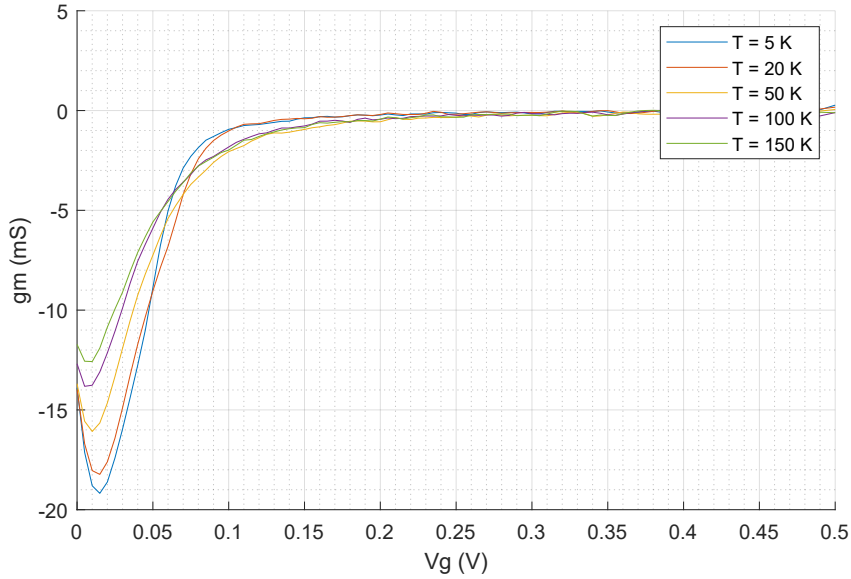


Figure 3.16: Trans-conductance of the device, computed under the same conditions as the current.

We notice that the simplified description of the screening we used in the previous chapter was more or less accurate, but the temperature had little effect on it. From this analysis we can see instead that the temperature has both the effect of increasing the total current, as it increases the number of carriers available in the material, and of reducing the gain, as the screening effect becomes stronger.

The same screening model could be also used to model a field effect transistor that modulates the charge in the channel, like what happens for semiconductor devices. In this case there is no potential barrier, and the gate covers the Weyl semimetal slab completely, tuning the amount of carriers in the underlying regions. Further work could be done towards the realization of such a model, in particular to better understand the transport properties of the surface and bulk states of the material, needed to describe the conductivity of the channel.

Chapter 4

Fabrication of test devices

The best way to test the validity of the physical models made in this work, as well as to further probe the properties of Weyl semimetals, is to compare the results of the simulations with some measurements made on a real device. To this purpose, in the last months of the thesis project, I assisted in the fabrication of a Weyl semi-metal field-effect test device. In this section the fabrication process that was used to realize this device is described.

4.1 Challenges in the fabrication of Weyl semimetal crystalline layers

Weyl semimetals are a class of materials that was discovered recently and their fabrication is still a challenging process. In particular, it is difficult to produce crystalline materials with good properties and purity. For this reason we can not yet use the regular deposition technique to deposit a Weyl semimetal layer on our devices, as the material realized in this way would not have the properties we desire.

However, it is currently possible to fabricate single crystals of macroscopic dimensions. As a result, the strategy we use to integrate these materials in a device is to cut a small portion from a large Weyl semimetal crystal, and to lay it on top of our device. The most suited instrument to perform this operation is the Focused Ion Beam, which uses a beam of charged ions to cut a thin lamella out of a sample. Using the same tool, the lamella can then be placed on a device, and some contacts can be soldered to it, having both the function of connecting it electrically and of keeping it in place.

This fabrication step is the most critical for our process, since operating the FIB requires a lot of time and a skilled operator. Moreover, this fabrication step must be repeated for each device we want to fabricate, meaning that it is feasible only

to produce single test devices; if these devices will ever be employed in a circuit a more standard fabrication process must be used. For these reasons it is best to perform the Focused Ion Beam step towards the end of the fabrication process, so that the single device produced is less likely to be damaged in the following steps.

With these considerations in mind, the fabrication process described in the following section was implemented.

4.2 Description of the fabrication process

The test devices were realized in the following way: the final transistor is placed upside-down on the wafer, with the channel on top and the electrodes below it, this allowed for the Weyl semimetal channel to be placed at the end of the process, when the rest of the device had already been completed.

We start with an oxide-capped wafer, where a thick silicon oxide layer covers the silicon top surface. The role of this oxide is to provide a good insulation, as we will deposit the contacts of our device on it.

The first contact to be deposited is the gate contact; in order to pattern the regions where it should be, a photoresist is first deposited on the oxide. The chosen photoresist is positive, meaning that the region of the surface that is exposed is the one that will be removed. It is also formed by two different layers, where the bottom one is more sensitive than the top one, so that when it is etched, the resulting cavity will be wider on the bottom than at the top.

The exposure is performed with a laser writer machine, which moves a laser beam on the surface of the sample to expose the selected areas. This machine does not use a mask, which makes it particularly suitable to fabricate single chips and try new designs. The region of the photoresist that is exposed becomes more soluble, and can be removed during the development step, leaving a cavity in the desired region.

The next step consists in depositing the metal layer using a physical vapor deposition technique: a crucible full of metal is heated, making some of it evaporate on the sample. The evaporation process is performed first with titanium, to form a thin layer, then with gold, to form the actual electrode and then again with titanium to form another thin film. The thin titanium layers have the role of favouring the adhesion of gold on silicon oxide and vice versa, while gold is used for the electrode as it has a lower resistivity.

The metallic layer deposited in this way will be in contact with the oxide surface only in the desired area, as the rest is still covered by the photoresist. Both metal and photoresist are then removed from the unwanted areas by lift-off, a process that consists in dissolving the remained photoresist and has the effect of also removing the metal deposited on top of it.

After the gate contact has been realized, a thin silicon oxide layer is deposited on the whole surface of the device, in order to insulate the gate contact from the Weyl semimetal slab that will be placed on top of it. A hole is then etched in the silicon oxide in order to contact the gate buried under it. This can be obtained with a lithography process similar to the one described before, with the difference that the resist this time is placed on top of the oxide and has the function of protecting it from the etching. Hence, the silicon oxide is removed only where the photoresist has been exposed.

The fabrication steps described up to now are illustrated in Figure 4.1:

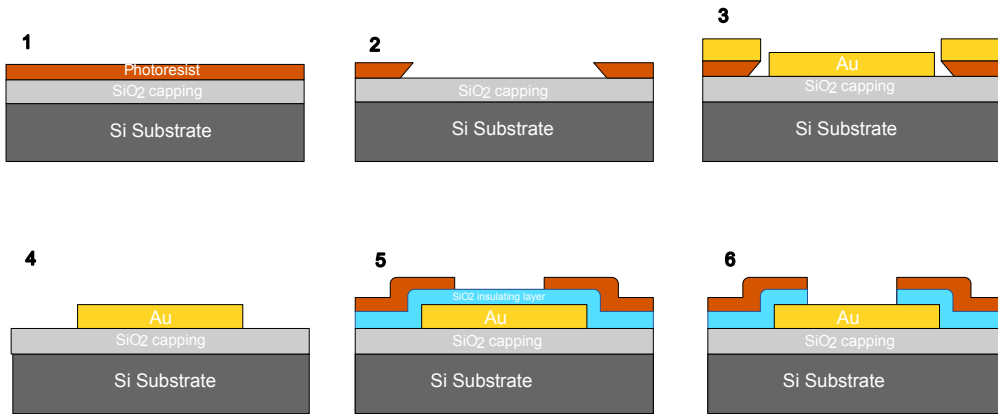


Figure 4.1: Steps used for the realization of the gold gate contact: step 1 represents the deposition of the photoresist, step 2 is the patterning with the laser writer and the subsequent developing, in step 3 the gold layer is deposited, in step 4 the remaining photoresist is stripped away, step 5 shows the deposition and patterning of a new layer of photoresist and step 6 shows represents the etched cavity in the oxide layer, used to electrically connect the gate contact.

The source and drain contacts are then deposited, using the same lift-off process used for the gate contact. They are deposited on top of the silicon oxide layer, since they need to be in contact with the channel. These contacts start from large metal pads and converge towards a central zone where the Weyl semimetal will be deposited. Some redundant contacts were added, in order to improve the likelihood of making a working device (since this is a relatively new fabrication process) and to allow the use of the sample for other kinds of measurements.

Now that the lithographic steps are complete the wafer is diced, separating one chip from the other. Then, the chips are inspected at the microscope in order to choose a good one, to carry on with the next step. In fact, the rest of the process is performed using the Focused Ion Beam, that allows to work on only one device at a time. We start with the preparation of a Weyl semimetal slab, which is cut from a large crystal using the Focused Ion Beam. The tool produces a beam of accelerated

Gallium ions that impinge on the surface of the sample, effectively cutting it. It is also possible to use a beam of low-energy ions that instead deposit on the surface of the sample. This technique allows to attach the Weyl semimetal slab cut from the crystal to a manipulator and place it on the device. Using the same technique, the slab is soldered to the existing source and drain contacts, in order to ensure a good electrical connection and to permanently fix it to the substrate. The last fabrication steps here described are shown in Figure 4.2:

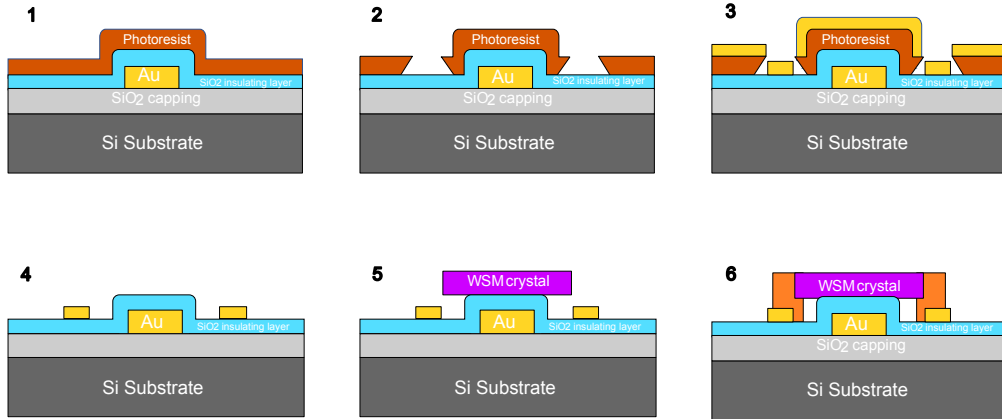


Figure 4.2: Schematic representation of the final steps of the fabrication process: steps 1 to 4 show the lithographic process used to make the source and drain contacts of the device, in step 5 the Weyl semimetal slab has been placed on the device, and in step 6 the slab is connected to the existing contacts. The cross section shown in this picture is rotated by 90° with respect to Figure 4.1.

Once the device is complete, the chip is placed on a holder that allows it to be connected to the measurement instrumentation. The electrical connection between the device and the holder is done via wire bonding, between the contact pads that we fabricated around the device and the holder pads. The final device, placed in its holder is shown in Figure 4.3. The characterization of the completed device will be carried out in the following months, and the results of such measurements will be useful as a reference for the physical models described in this work.

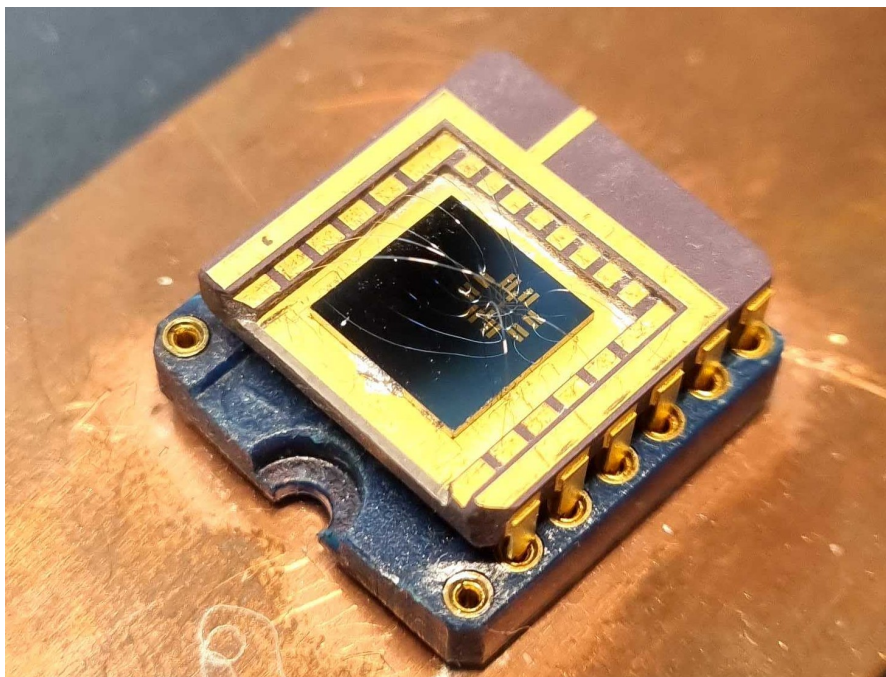


Figure 4.3: Photography of the final device ready to be tested.

Chapter 5

Conclusions

Topological materials, and in particular Weyl semimetals, show many peculiar properties, some of which make them promising candidates for electronic applications, especially in a cryogenic environment. For this reason, this work was oriented towards the modeling of electronic devices that exploit these unique properties, with the goal to study and realize novel field-effect transistors. We focused our attention in particular on the class of type-I Weyl semimetals.

We started this work by illustrating the concept of a Klein tunneling transistor, and our analysis pointed out that the strong screening of the electric field is an important factor in determining the performance of such a device.

Then, we focused more on the screening effect, in order to obtain a more precise description of the phenomenon, including both the external conditions and the properties of the material. The result was a quantitative description of the screening effect in Weyl semimetals together with the study of the effect of several physical parameters on this phenomenon, like the temperature which increases the intensity of the screening effect, the position of the Fermi level of the material and the length of the Fermi arcs. We were also able to compute the charge density in the channel as an effect of the potential applied, distinguishing between the contribution of the bulk and surface states, and to provide an estimation of the resulting gate capacitance.

This study provides us additional information on the properties of Weyl semimetals and shows that, although screening is a quite strong effect in Weyl semimetals, it is possible in sufficiently scaled devices to use a gate as an effective control mechanism.

The developed model can be used in the future as part of models of field-effect transistors, in order to evaluate their performances. We provide an example of its application by employing it to improve the description of the Klein tunneling device presented previously, in place of the simplified description of screening that was previously used.

Finally, we described part of the ongoing work aimed at the realization of test devices, that will allow to study experimentally the properties of Weyl semimetals.

The next step is the characterization of such devices, in order to compare the results of the simulations with some experimental data. This will provide more information on the accuracy of the models used, as well as additional insight on the operation of the real devices, and on other effects that may influence their behavior.

Appendix A

Numerical methods used to solve the Poisson differential equation

In this appendix we will describe the methods used in order to solve the Poisson equation. As said in the previous sections, because of the description we used for the Fermi Arc states, we obtained an expression of the surface density of states that does not have a closed form. The surface density of states appears in the Poisson differential equation that describes the decay of the potential in the Weyl semimetal layer, and for this reason, it was necessary to solve it numerically.

Furthermore, the boundary conditions we found are located at the two extremes of the interval where the solution must be defined. These boundary conditions define what is called a Boundary Value Problem, that is generally harder to solve than the more common Initial Value Problem in which the boundary conditions are defined in the same spot. It is also important to note that the presence of two boundary conditions in this case does not guarantee that the solution exists or that it is unique.

A.1 Solution as a series of Initial Value Problems

The first approach used to solve the differential equation was to employ an algorithm for the solution of initial value problems used in an iterative way, until a solution satisfying all the requirements was found. The advantage is that these algorithms are relatively easy to implement, and some of them are already implemented in MATLAB [45].

The boundary condition defined in Equation 3.23 does not allow to directly

determine the value of either $U(0)$ or $U'(0)$ but gives only the relationship between the two. As a result, both the initial values must be guessed and later corrected to get closer to the desired ones. We can start by guessing the value of $U(0)$, since we know that it will be necessarily smaller than the voltage V_g applied on the gate. We can then use Equation 3.23 to compute the value of the derivative $U'(0)$ that satisfies it, since this equation is linear there will be only one solution. Now we have both initial conditions, and we can proceed to solve the differential equation with our Initial Value Problem solver algorithm. The outputs will be the values of the function $U(x)$ and of its derivative in every point of the selected interval. We then check if the other boundary condition (Equation 3.24) is satisfied; if it is not the case, we need to try again with a different value of $U(0)$.

The second boundary condition reads $U(x = \text{WSM thickness}) = 0$, where the function $U(x)$ depends on the value of $U(0)$, we could then treat it like an unknown function of which we are trying to find a zero: $U(x = \text{WSM thickness}) = f(U(0)) = 0$, this can be solved with a common root-finding algorithm. The simplest example of such algorithm is the bisection method, which consists in probing the interval where the zero is located, by checking the middle point of the interval and excluding one of the two halves from the search. In fact, we know that the input value must be in the interval $V_g \geq U(0) \geq 0$; if, as we expect there is a single solution located in this interval when computing $f(V_g)$ and $f(0)$ we will get two values with opposite sign. We can then check the sign of $f(V_g/2)$ which is the middle point of the interval, we know that the zero will be necessarily located between two points of opposite signs. We can then repeat this procedure on subsequent intervals to locate more and more precisely the position of the zero. Once we are satisfied with the accuracy we have obtained our solution $U(x)$ that satisfies both boundary conditions.

Figure A.1 summarizes the main steps of the described algorithm:

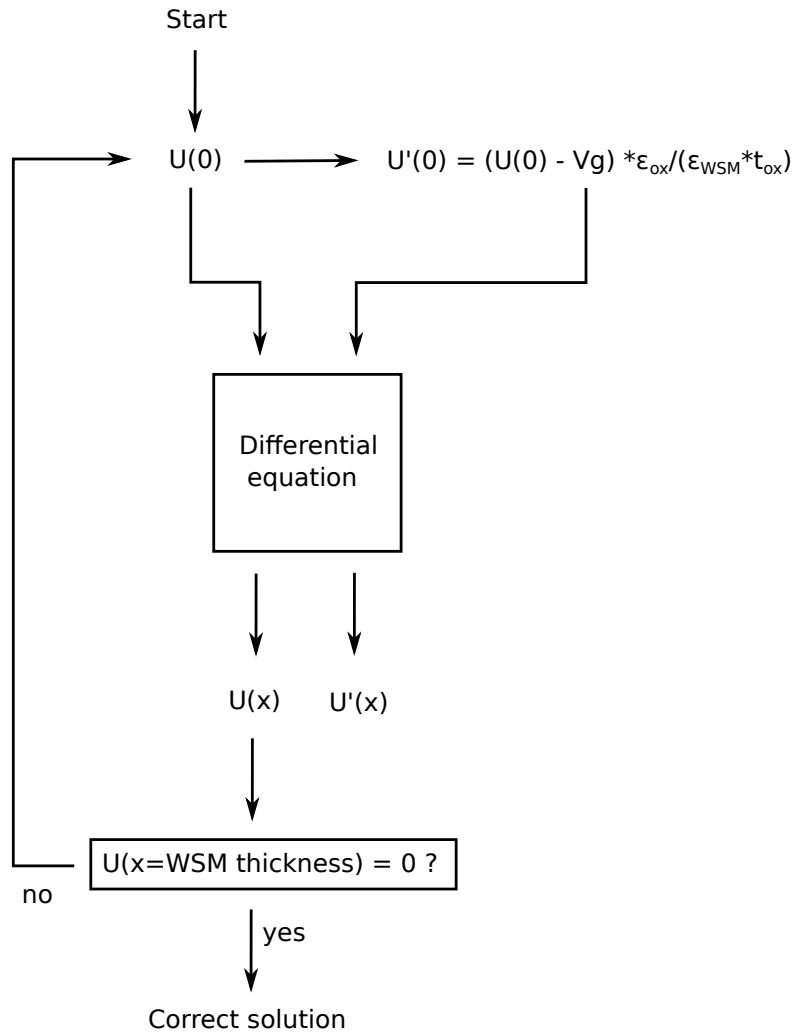


Figure A.1: Scheme of the algorithm used to solve the Poisson differential equation, by calling a regular ODE solver iteratively, until a solution that checks both boundary conditions is found.

The main drawback of this technique is that many iterations are needed to reach the desired solution, so the overall algorithm is relatively slow. Another issue is that, given the type of functions studied, a small imprecision on the values of $U(0)$ and $U'(0)$ leads to a large change in the values on the other side of the interval, like $U(x = \text{WSM thickness})$ that we are using to check for the correct solution. Therefore sometimes the algorithm is limited on the maximum number of digits that can be used to describe the initial conditions, and might not be able to satisfy small tolerances set on the check of the result.

For this reasons, although the results were acceptable, the presented solution was later replaced by an alternative tool that is already implemented in MATLAB. Its working principles are illustrated in the following section.

A.2 Direct solution of the Boundary Value Problem

MATLAB already has an integrated Boundary Problem Solver called `bvp4c`. It is based on a Runge-Kutta method, which belongs to the family of finite difference methods [46]. These are algorithms where the derivative of a function in one point is approximated with the finite difference of the values of the function in some points close to it [47]. In fact, these algorithms estimate the solution only in a set of discrete points along interval, that are called grid points or mesh points. Two grid points are the extremes of the interval, and the value of the solution there is given by the boundary conditions, in the other points between them the value has to be computed. A simple finite difference formula is the centered difference approximation, that allows to approximate the second derivative in the following way:

$$D^2[U(x_j)] = \frac{U(x_{j+1}) - 2U(x_j) + U(x_{j-1}))}{h^2} \quad (\text{A.1})$$

Where $U(x)$ is the solution function, x_j are the points of the grid and h is the spacing between them. This allows to transform the Poisson differential equation into an algebraic equation. If we apply this equation to each of the grid points we obtain a system of equations, that can be solved to obtain an approximate evaluation of the solution at the grid points. These values can be then interpolated to evaluate the solution at any possible point.

Bibliography

- [1] The Nobel Foundation. *The Nobel Prize in Physics 2016*. 2016. URL: <https://www.nobelprize.org/prizes/physics/2016/press-release/>.
- [2] Binghai Yan and Claudia Felser. «Topological Materials: Weyl Semimetals». In: *Annual Review of Condensed Matter Physics* 8.1 (Mar. 31, 2017).
- [3] Joel E. Moore. «The Birth of Topological Insulators». In: *Nature* 464.7286 (7286 Mar. 2010).
- [4] Satyaki Kar and Arun M. Jayannavar. «A Primer on Weyl Semimetals: Down the Discovery of Topological Phases». In: *Asian Journal of Research and Reviews in Physics* (Feb. 18, 2021).
- [5] Haijun Zhang, Chao-Xing Liu, Xiao-Liang Qi, Xi Dai, Zhong Fang, and Shou-Cheng Zhang. «Topological Insulators in Bi_2Se_3 , Bi_2Te_3 and Sb_2Te_3 with a Single Dirac Cone on the Surface». In: *Nature Physics* 5.6 (6 June 2009).
- [6] J. González and R. A. Molina. «Topological Protection from Exceptional Points in Weyl and Nodal-Line Semimetals». In: *Physical Review B* 96.4 (July 31, 2017).
- [7] N. P. Armitage, E. J. Mele, and Ashvin Vishwanath. «Weyl and Dirac Semimetals in Three-Dimensional Solids». In: *Reviews of Modern Physics* 90.1 (Jan. 22, 2018).
- [8] Pavan Hosur and Xiaoliang Qi. «Recent developments in transport phenomena in Weyl semimetals». In: *Comptes Rendus Physique* 14.9-10 (Nov. 2013).
- [9] Yuriko Baba, Álvaro Díaz-Fernández, Elena Díaz, Francisco Domínguez-Adame, and Rafael A. Molina. «Electric field manipulation of surface states in topological semimetals». In: *Physical Review B* 100.16 (Oct. 3, 2019).
- [10] Nitesh Kumar et al. «Extremely high magnetoresistance and conductivity in the type-II Weyl semimetals WP2 and MoP2». In: *Nature Communications* 8.1 (Nov. 21, 2017).

-
- [11] Chandra Shekhar et al. «Extremely large magnetoresistance and ultrahigh mobility in the topological Weyl semimetal candidate NbP». In: *Nature Physics* 11.8 (Aug. 2015).
- [12] Davide Grassano, Olivia Pulci, Adriano Mosca Conte, and Friedhelm Bechstedt. «Validity of Weyl fermion picture for transition metals monpnictides TaAs, TaP, NbAs, and NbP from ab initio studies». In: *Scientific Reports* 8.1 (Feb. 23, 2018).
- [13] Zhenwei Wang, Kaifa Luo, Jianzhou Zhao, and Rui Yu. «Large Fermi arc and robust Weyl semimetal phase in Ag_2S ». In: *Physical Review B* 100.20 (Nov. 12, 2019).
- [14] M.-Y. Yao et al. «Observation of Weyl Nodes in Robust Type-II Weyl Semimetal WP_2 ». In: *Physical Review Letters* 122.17 (May 3, 2019).
- [15] Jorrit C. de Boer, Daan H. Wielens, Joris A. Voerman, Bob de Ronde, Yingkai Huang, Mark S. Golden, Chuan Li, and Alexander Brinkman. «Nonlocal Signatures of the Chiral Magnetic Effect in the Dirac Semimetal $\text{Bi}_{0.97}\text{Sb}_{0.03}$ ». In: *Physical Review B* 99.8 (Feb. 13, 2019).
- [16] Shun-Qing Shen. «Topological Dirac and Weyl Semimetals». In: *Topological Insulators: Dirac Equation in Condensed Matter*. Ed. by Shun-Qing Shen. Springer Series in Solid-State Sciences. Singapore: Springer, 2017, pp. 207–229.
- [17] Zhijun Wang, Hongming Weng, Quansheng Wu, Xi Dai, and Zhong Fang. «Three Dimensional Dirac Semimetal and Quantum Transports in Cd_3As_2 ». In: *Physical Review B* 88.12 (Sept. 23, 2013).
- [18] Ratnadwip Singha, Arnab Kumar Pariari, Biswarup Satpati, and Prabhat Mandal. «Large nonsaturating magnetoresistance and signature of nondegenerate Dirac nodes in ZrSiS ». In: *Proceedings of the National Academy of Sciences* 114.10 (Mar. 7, 2017).
- [19] C. L. Kane and E. J. Mele. «Quantum Spin Hall Effect in Graphene». In: *Physical Review Letters* 95.22 (Nov. 23, 2005).
- [20] Serguei Tchoumakov, Marcello Civelli, and Mark O. Goerbig. «Magnetic Description of the Fermi Arc in Type-I and Type-II Weyl Semimetals». In: *Physical Review B* 95.12 (Mar. 8, 2017).
- [21] Yuya Ominato and Mikito Koshino. «Quantum transport in three-dimensional Weyl electron system». In: *Physical Review B* 89.5 (Feb. 6, 2014).
- [22] B. Q. Lv et al. «Observation of Fermi-Arc Spin Texture in TaAs». In: *Physical Review Letters* 115.21 (Nov. 16, 2015).

-
- [23] Alexey A. Soluyanov, Dominik Gresch, Zhijun Wang, QuanSheng Wu, Matthias Troyer, Xi Dai, and B. Andrei Bernevig. «Type-II Weyl Semimetals». In: *Nature* 527.7579 (7579 Nov. 2015).
- [24] Ryo Okugawa and Shuichi Murakami. «Dispersion of Fermi arcs in Weyl semimetals and their evolutions to Dirac cones». In: *Physical Review B* 89.23 (June 20, 2014).
- [25] Giacomo Resta, Shu-Ting Pi, Xiangang Wan, and Sergey Y. Savrasov. «High surface conductivity of Fermi-arc electrons in Weyl semimetals». In: *Physical Review B* 97.8 (Feb. 22, 2018).
- [26] Maxim Breitkreiz and Piet W. Brouwer. «Large Contribution of Fermi Arcs to the Conductivity of Topological Metals». In: *Physical Review Letters* 123.6 (Aug. 9, 2019).
- [27] B. Q. Lv et al. «Experimental Discovery of Weyl Semimetal TaAs». In: *Physical Review X* 5.3 (July 31, 2015).
- [28] R. D. Y. Hills, A. Kusmartseva, and F. V. Kusmartsev. «Current-Voltage Characteristics of Weyl Semimetal Semiconducting Devices, Veselago Lenses and Hyperbolic Dirac Phase». In: *Physical Review B* 95.21 (June 5, 2017).
- [29] Chunxu Bai, Yanling Yang, and Ke-Wei Wei. «A wavevector filter in inversion symmetric Weyl semimetal». In: *Physics Letters A* 380.5 (Feb. 15, 2016).
- [30] Yaohua Tan, Mirza M. Elahi, Han-Yu Tsao, K. M. Masum Habib, N. Scott Barker, and Avik W. Ghosh. «Graphene Klein tunnel transistors for high speed analog RF applications». In: *Scientific Reports* 7.1 (Aug. 29, 2017).
- [31] M. I. Katsnelson, K. S. Novoselov, and A. K. Geim. «Chiral tunnelling and the Klein paradox in graphene». In: *Nature Physics* 2.9 (Sept. 2006).
- [32] N. Stander, B. Huard, and D. Goldhaber-Gordon. «Evidence for Klein Tunneling in Graphene $p - n$ Junctions». In: *Physical Review Letters* 102.2 (Jan. 16, 2009).
- [33] Quentin Wilmart, Salim Berada, David Torrin, V. Hung Nguyen, Gwendal Fève, Jean-Marc Berroir, Philippe Dollfus, and Bernard Plaçais. «Klein-tunneling transistor with ballistic graphene». In: *arXiv:1409.6170 [cond-mat]* (Sept. 22, 2014).
- [34] Redwan N. Sajjad and Avik W. Ghosh. «Manipulating Chiral Transmission by Gate Geometry: Switching in Graphene with Transmission Gaps». In: *ACS Nano* 7.11 (Nov. 26, 2013).
- [35] Devashish Pandey, Matteo Villani, Enrique Colomés, Zhen Zhan, and Xavier Oriols. «Implications of the Klein tunneling times on high frequency graphene devices using Bohmian trajectories». In: *Semiconductor Science and Technology* 34.3 (Feb. 2019).

- [36] Zhuo Bin Siu, Can Yesilyurt, Mansoor B. A. Jalil, and Seng Ghee Tan. «Influence of Fermi arc states and double Weyl node on tunneling in a Dirac semimetal». In: *Scientific Reports* 7.1 (June 22, 2017).
- [37] M. Ramezani Masir, P. Vasilopoulos, and F. M. Peeters. «Fabry-Pérot resonances in graphene microstructures: Influence of a magnetic field». In: *Physical Review B* 82.11 (Sept. 10, 2010).
- [38] Manik Goyal, Luca Galletti, Salva Salmani-Rezaie, Timo Schumann, David A. Kealhofer, and Susanne Stemmer. «Thickness dependence of the quantum Hall effect in films of the three-dimensional Dirac semimetal Cd_3As_2 ». In: *APL Materials* 6.2 (Feb. 1, 2018).
- [39] Yanwen Liu et al. «Gate-tunable quantum oscillations in ambipolar Cd_3As_2 thin films». In: *NPG Asia Materials* 7.10 (Oct. 2015).
- [40] Songci Li and A. V. Andreev. «Spiraling Fermi arcs in Weyl materials». In: *Physical Review B* 92.20 (Nov. 19, 2015).
- [41] Neil W. Ashcroft and N. David Mermin. *Solid state physics*. New York: Holt, Rinehart and Winston, 1976. 826 pp.
- [42] Zhijun Wang, Yan Sun, Xing-Qiu Chen, Cesare Franchini, Gang Xu, Hongming Weng, Xi Dai, and Zhong Fang. «Dirac semimetal and topological phase transitions in $A_3\text{Bi}$ ($A = \text{Na}, \text{K}, \text{Rb}$)». In: *Physical Review B* 85.19 (May 22, 2012).
- [43] R. D. Shannon. «Dielectric polarizabilities of ions in oxides and fluorides». In: *Journal of Applied Physics* 73.1 (Jan. 1, 1993).
- [44] S. A. Kulinich, M. E. Leonova, L. G. Sevast'yanova, O. K. Gulish, and K. P. Burdina. «High-Pressure Synthesis of Sodium Bismuthide Na_3Bi ». In: *Russian Journal of General Chemistry* 69 (May 1, 1999).
- [45] Lawrence F. Shampine and Mark W. Reichelt. «The MATLAB ODE Suite». In: *SIAM Journal on Scientific Computing* 18.1 (Jan. 1, 1997).
- [46] Jacek Kierzenka and Lawrence F. Shampine. «A BVP solver based on residual control and the Matlab PSE». In: *ACM Transactions on Mathematical Software* 27.3 (Sept. 1, 2001).
- [47] Uri M. Ascher, Robert M. M. Mattheij, and Robert D. Russell. *Numerical Solution of Boundary Value Problems for Ordinary Differential Equations*. Classics in Applied Mathematics. Society for Industrial and Applied Mathematics, Jan. 1, 1995. 618 pp.